Interfacial and Nanoscale Science Facility

The Interfacial & Nanoscale Science (I&NS) Facility is a world-class resource for scientific expertise and instrumentation focused on the study of interfacial phenomena and nanoscience and technology. This section summarizes the capabilities available in the I&NS Facility, along with research programs associated with facility users. Activities in the I&NS Facility address national needs in environmental restoration, waste management, pollution prevention, energy, and national security through research that specializes in preparation, characterization, interactions, and reactivity of interfaces and nanoscale materials. The range of scientific expertise and instrumentation within the I&NS Facility provides a unique environment for research in areas such as nanoscience and nanotechnology, heterogeneous catalysis, environmental interfaces including aerosols and minerals, materials and chemoselective interfaces, and areas within microanalytical science such as chemical sensing and nanobiotechnology.

The I&NS Facility and its scientific staff provide a broad range of instrumentation, laboratory capabilities, and expertise. Instrumentation is available for chemical synthesis, analytical chemistry, separations, electrochemistry, thin film deposition, catalytic reactors, ion-beam processing, and microfabrication. Capabilities include an accelerator facility for material modification and analysis using ion beams along with interface characterization; scanning probe microscopies; electron microscopy and x-ray analysis; spectroelectrochemistry; high-spatial/energy resolution surface analysis; catalyst preparation, characterization, and reaction engineering; a fully equipped clean room for microfabrication, microanalytical systems development and testing laboratories; inorganic, organic, polymer, and biochemical synthesis and characterization facilities; a full complement of thin-film deposition and characterization facilities; and fully equipped analytical support laboratories. The combination of surface and interface characterization techniques that provide high spatial, depth, and energy resolution for a broad array of methods is unmatched anywhere in the world. Many systems are coupled directly to film growth chambers, and samples can be moved among 16 different systems under controlled environment without exposure to air.

Instrumentation & Capabilities

- Thin-film deposition
- Surface analysis suite
- Electron microscopy suite
- Scanning probe microscopy
- Ion-beam processing and analysis
- Nanobiotechnology capabilities
- Surface science and catalysis laboratory
- Catalytic reactors
- X-ray diffraction laboratory
- Microfabrication
- Chemical and biological sensing
- Other analytical and characterization laboratories

Staff assigned to the I&NS Facility perform innovative research in the areas of surface and interfacial chemistry, advanced materials synthesis and characterization, and microanalytical science. Our activities emphasize research relevant to the four U.S. Department of Energy (DOE) mission areas–science, energy resources, environmental quality, and national security–and to operation of a world-class user facility for scientific problem-solving that supports DOE's science mission. Our staff also plays a major role in the continued success of the W.R. Wiley Environmental Molecular Sciences Laboratory (EMSL) by providing

support, training, and collaboration to onsite users. Over the past seven years, research activities in the I&NS Facility have focused on four major thrust areas: 1) films and interphases, 2) surface chemistry and catalysis, 3) material interfaces, and 4) microsensors, microfluidics, and new biotechnologies. Staff assigned to the I&NS Facility continue to focus their efforts in these four areas with research on the following topics:

- *Oxide and Mineral Films and Surfaces*. Structural and chemical properties of model single-crystal oxide and complex mineral surfaces.
- *Electronic and Catalytic Materials*. High dielectric materials, magnetic oxide semiconductors, and oxide catalysts.
- *Nanoscale Materials*. Oxide quantum dots and nanofilms of magnetic and oxygen ion-conducting oxides, buried nanoclusters in oxides.
- *Interfacial Properties and Reactivity*. Reactions at oxide and mineral interfaces and the structural and chemical properties.
- *Microanalytical Separations and Sensing*. Development of new microanalytical and sensing principles, tools, and testing.
- *Nanobiotechnology*. Single-enzyme nanoparticles, enzymes in nanostructured matrices, understanding the dynamics of these materials.
- *Environmental Studies*. Waste separations, structural and chemical stability of waste forms under different radiation and chemical environment, atmospheric aerosols.
- *Analysis and Characterization*. Fully equipped analytical laboratories and characterization facilities.

Films and Interphases. The physical and chemical properties of the region between single phases of a material (i.e., the interphase) have a major influence on many characteristics of the material, including stability, electronic properties, atomic and ionic transport, and chemical reactivity. Research programs include the synthesis of thin films and nanostructured materials, both of which contain a high concentration of interphase regions. Research activities also involve studies of solid/solid, solid/liquid, and solid/gas (or vacuum) interphase regions. Although most studies are focused on inorganic materials and interphases, organic and biological systems are becoming an increasingly large part of our work.

Surface Chemistry and Catalysis. Basic research is carried out with the most simple, well-defined, environmentally relevant crystallographic structures (e.g., mineral carbonates, metal oxides) for which molecular theory and spectroscopy are immediately applicable. The work then progresses to materials with more complex structures, such as iron and titanium oxides with substitutional impurities. For example, fundamental studies of the oxygen storage and release properties of pure and zirconium-doped ceria single-crystal thin films are aimed at understanding how these 'oxygen storage materials' perform in an automobile exhaust catalytic converter. In addition to fundamental surface chemistry research, we are developing materials and reactor designs for a number of heterogeneous catalytic processes. One study involves synthesizing, characterizing, and testing a group of novel, mesoporous silica-supported, solid-acid catalysts for use in petroleum refining processes.

Material Interfaces. Studies are being conducted in several areas: solid/solid interfaces in a wide variety of materials, radiation effects in materials, fundamental defect properties and

interactions, atomic and ionic transport, and aerosol characterization. Many of the studies on solid/solid interfaces involve 1) characterization of interfaces between thin films and substrates, between ion-beam-modified surfaces and the original substrate, or between nanoclusters and host matrices; 2) segregation or diffusion of point defects, impurities, dopants, or gas atoms to or from such interfaces; 3) transport of hydrogen, oxygen, or other gases across such interfaces; 4) formation or destruction of such interfaces from radiation damage processes; and 5) stability of interfaces under a wide range of environmental conditions. Studies on radiation effects include experimental research on materials for immobilization of nuclear waste and plutonium, as well as materials for next-generation nuclear power production, wide-band-gap semiconductors, and multiscale computer simulations of damage production processes, defect diffusion, and microstructure evolution. Studies on atomic and ionic transport include ion exchange processes in nuclear waste glasses, hydrogen storage and transport in materials, and oxygen transport in fast ion conductors.

Microsensors, Microfluids, and Nanobiotechnology. This research includes four primary thrust areas: 1) array-based vapor sensors, 2) nanoscience, 3) bioanalytical micro-fluidics, and 4) radioanalytical microfluidics. Key areas of science in array-based vapor sensing include rational design, development, and synthesis of polymeric sensing materials, linear free-energy models for vapor/polymer interactions, organic thin films, photo-patterning methods for sensor materials, integrated sensor systems, and multivariate data analyses. The nanoscience area includes development of monolayer-protected gold nanoparticles for use on sorptive sensing films, single-enzyme nanoparticles as a new nanostructure for enzyme stabilization, and multi-functional nanoparticle assemblies for biodetection. The latter two areas represent a new thrust in nanobiotechnology, and a laboratory within EMSL has been established for synthesizing enzyme nanostructures and studying enzyme kinetics and enzymes in nanostructured matrices. Experimental research in bioanalytical micro-fluidics and radioanalytical microfluidics is now located primarily in other facilities, but close scientific ties with EMSL are maintained.

Capabilities

Thin Film Deposition. Thin film deposition capabilities include oxygen plasma-assisted molecular beam epitaxy (MBE) systems, a metal organic chemical vapor deposition system (MOCVD), and a sputter deposition system. The MBE systems consist of growth chambers connected to surface characterization chambers through sample transfer lines. The growth chambers have various electron beam and effusion cell sources along with reflection high-energy electron diffraction (RHEED) and quartz crystal oscillators to monitor the growth. The surface characterization chambers are equipped with several surface science capabilities including x-ray photoelectron spectroscopy (XPS)/diffraction (XPD), Auger electron spectroscopy (AES) low-energy electron diffraction (LEED), and atomic force microscopy/scanning tunneling microscopy (AFM/STM). The MOCVD system is specially designed for epitaxial growth of oxide thin films. The system comprises a rotating disk reactor, two metal organic source delivery systems (bubbler vapor-phase and direct liquid source-injection), an oxygen microwave plasma unit, a spectroscopic ellipsometer, and a Fourier transform infrared (FTIR) spectrometer. The system is capable of growing uniform (in both thickness

and composition) oxide thin films with abrupt interfaces. The sputter deposition system consists of radio frequency and direct current sputtering sources.

Surface Analysis Suite. The surface analysis suite consists of a Physical Electronics Instruments (PHI) Quantum 2000 high-resolution, x-ray photoelectron spectrometer (pictured in Figure 1), a Kratos Axis multi-technique surface analysis system (SAS), a PHI Model T2100 time-of-flight secondary ion mass spectrometer (TOF-SIMS), and a PHI Model 680 AES/scanning Auger microprobe. The Quantum 2000 XPS system is unique in that it uses a focused monochromatic Al K α x-ray beam that can be varied in size from as small as 10 μm in diameter to approximately 200 μm. The TOF-SIMS system uses a pulsed and focused ion source and TOF analyzer to obtain high spatial- and mass-resolution data from a specimen surface. The multi-technique SAS enables surfaces to be probed with a variety of complementary analysis methods, and contains electron imaging, electron spectroscopy, and both primary and secondary ion-scattering capabilities. The Model 680 AES/scanning Auger microprobe is based on a field emission electron source and a cylindrical mirror analyzer. The electron beam size can be focused as low as 10 nm at 20 kV, although somewhat larger beams are typically used to collect AES data. Instrument features and capabilities include beam rastering, scanning electron microscope (SEM) imaging, mapping, specimen cleaning and depth profiling using a sputter gun, and sample rotation to allow "Zalar" rotation during sputtering. The system also is configured with an x-ray detector for near-surface analysis in combination with AES surface analysis.

Figure 1. X-ray photoelectron spectrometer.

Electron Microscopy Suite. The electron microscopy suite consists of a LEO 982 field-emission scanning electron microscope (FESEM), a high-resolution transmission electron microscope (TEM), and an environmental scanning electron microscope (ESEM). The FESEM is an ultra-high-performance SEM with a resolution of 1 nm at 30 kV and 4 nm at 1.0 kV. It has a large specimen chamber equipped with multiple detectors, a below-lens secondary electron detector, an in-lens secondary electron detector, a backscatter electron detector, an energy dispersive x-ray detector, and an electron backscatter diffraction detector. The JEOL 2010 is a high-resolution TEM with a spatial resolution of 0.194 nm. This instrument has a medium acceleration voltage of 200 kV, a high-brightness electron source, digital image recording, a computer-controlled sample goniometer, and a geometrically optimized x-ray detector. It has a wide range of illumination lens conditions: TEM mode, energy dispersive spectroscopy mode, nanometer beam electron diffraction (NBED), and convergent beam electron diffraction (CBED). The TEM is post-column attached with a Gatan image filter, giving an optimized energy resolution of approximately 1.2 eV, which allows analysis of light elements by electron energy-loss spectroscopy (EELS) and elemental mapping in the electron spectroscopic imaging (ESI). The ESEM is a high-performance, variable-pressure SEM with a resolution of 5 nm at 30 kV. It can be used to examine uncoated, non-conductive specimens, and with a Peltier stage, it can be used with wet

specimens. It will image specimens in a variety of atmospheres, such as water vapor, air, argon, nitrogen, and helium. The ESEM has a large specimen chamber equipped with an energy dispersive x-ray detector, a microinjector, and a micromanipulator.

Scanning Probe Microscopy. The scanning probe microscopy laboratory has a Digital Instrument Nanoscope IIIa AFM, a Topometrix TMX 1000 Explorer SPM, and a OmiCron variable noncontact ultra-high vacuum (UHV) AFM/STM system with surface science capabilities including XPS, Auger electron microscopy, plasma cleaning, and deposition. The instrument is capable of operating in both air and liquid environments and in several modes that include contact, tapping, frictional force, phase/frequency, capacitance, and magnetic/electrostatic force. As a real space probe, the instrument can be used to probe surface morphology, defects, and electrostatic, magnetic, dopant concentration, and mechanical properties of conducting and non-conducting materials. The Topometrix TMX 1000 Explorer SPM can be used for both AFM and STM in air and in liquid and is particularly useful for larger samples. This instrument includes both contact and non-contact (NC) AFM modes. STM requires an electrically conductive sample and produces images based on the topography and electronic structure of the sample. AFM samples may be insulating or conducting; the image is based on the force between the AFM probe and the sample and is primarily a map of the surface topography. The OmiCron variable scanning probe microscope can be used for both STM and AFM under UHV conditions. As a real space probe, this instrument is designed to probe surface structure, defects, and morphology of conducting and non-conducting materials. In addition to STM/AFM, the vacuum system also is equipped with other surface science capabilities that include LEED, XPS, AES, and oxygen plasma cleaning.

Ion Beam Processing and Analysis. The accelerator facility is equipped with capabilities to perform material modification and analysis using high-energy ion beams. The facility has two ion sources, a 3-MeV tandem ion accelerator, injector and analyzing magnets, beam lines, and four end stations. The end station on the +30° beam line is equipped with LEED, AES, XPS, oxygen plasma, and sputter cleaning sources and effusion cells in addition to the conventional ion beam capabilities. Ion beam capabilities include fixed and movable detectors for Rutherford backscattering spectrometry/channeling (RBS/C), nuclear reaction analysis (NRA), and elastic recoil detection analysis (ERDA). This beam line extends through the end station to another end station where experiments can be performed with the beam size of 20 microns or greater. The micro-beam end station is also equipped with capabilities for conventional ion beam techniques including RBS, NRA, and proton-induced x-ray emission (PIXE). The +15° beam line is equipped with a raster scanner for ion implantation and ion beam modification of materials, and the end station is equipped with all the conventional ion beam capabilities. The -15° end station is designed to carry out routine analytical work. The NEC RC 43 end station attached to this beam line is equipped with most of the standard ion beam analytical capabilities including RBS, NRA, PIXE, particle-induced gamma emission (PIGE), proton elastic scattering analysis, scanning transmission ion microscopy (STIM), and ERDA.

Surface Science and Catalysis Laboratory. Three UHV surface chemistry systems designed for studies of the molecular-level chemistry of adsorbates on metal oxide surfaces are available in the Surface Science and Catalysis Laboratory. These systems are equipped with a number of spectroscopic tools to follow changes in adsorbate chemistry, including

high-resolution electron energy loss spectroscopy (HREELS), SIMS, ultraviolet photoemission (UPS), XPS, AES, and LEED. In addition, both electron-stimulated desorption (ESD) and temperature-programmed desorption (TPD) studies are routinely performed in some systems. Typical information obtainable in TPD experiments includes the quantity and nature (intact or dissociated molecule) of an adsorbed gas. In addition, estimates of the sticking coefficient and the activation energy for desorption and/or reaction of the adsorbed molecule can be made. One of these systems has a combination of surface science and high-pressure catalysis capabilities and is capable of measuring gas/solid reaction rates under realistic, high-pressure (approximately1 atm) conditions using model, low-surface-area solid samples. Reaction rates as a function of temperature and varying reagent partial pressures also can be measured in this system.

Catalytic Reactors. The Reaction Engineering Laboratories are equipped with a variety of analytical capabilities and catalytic reactors including an Advanced Scientific Designs, Inc. RXM-100 catalyst testing and characterization instrument and a Zeton Altamira reactor test stand. The RXM-100, a multi-functional instrument used for catalyst studies, combines UHV and high-pressure capabilities in a single instrument without compromising specifications or ease of use. A number of measurements can be made using this instrument including chemical adsorption, physical adsorption, surface area, pore size, pore distribution, and temperature programmed characterization (desorption, reduction, and oxidation). An on-line mass spectrometer, gas chromatograph, FTIR, and thermal conductivity detector can be used to analyze effluent gases. The instrument has the capability of running up to 10 different gases simultaneously. In addition, high-pressure reactions (up to 1000 psi) can be run within a few minutes of each other on the same system, with little change in system configuration. This system offers extensive flexibility in catalyst testing and decreases inefficiency and contamination problems that arise from transferring materials between systems and waiting for data from other sources. The Zeton Altamira reactor test stand comprises three types of reactors generally used in bench-scale testing of catalysts: a fixed bed reactor, a Rotoberty reactor, and a continuous stirred tank reactor. This design allows users to evaluate catalyst performance and study chemical reactions in various reactor configurations.

X-Ray Diffraction. The suite of x-ray diffraction (XRD) equipment in EMSL consists of four instruments: a general-purpose XRD system for studying polycrystalline samples under ambient conditions, a special applications XRD system with low- and high-temperature sample stages covering the range of -193°C to +1000°C, and a four-circle XRD system. The general-purpose system is most often used to examine powder samples (x-ray powder diffraction [XRPD]), but it also can be used to study certain types of thin films. In addition to its non-ambient capabilities, the special applications system is equipped to examine thin-film samples in more detail, including grazing-incidence XRD (GIXRD) and x-ray reflectivity (XRR) measurements. The four-circle system is typically configured for high-resolution x-ray diffraction (HRXRD) studies of epitaxial thin films. Additional applications of the four-circle system include stress measurements, texture analysis, GIXRD, and XRR.

Chemically Selective Materials and Sensors. Development and evaluation of sensor materials and chemical microsensors are supported by a wet chemistry laboratory for organic, polymer, and nanomaterial synthesis; a laboratory for evaluation of chemical sensor and sensor materials using automated vapor generation and blending systems; and a clean

room with selected microfabrication capabilities. A variety of techniques for applying sensing materials to sensor devices are available, and numerous electronic test instruments are available in the sensing laboratories and the EMSL Instrument Development Laboratory. These capabilities are complemented by a range of surface analysis and characterization instruments as well as conventional analytical instrumentation in EMSL. Users may wish to bring new sensing materials to EMSL for application to sensing devices and evaluation, while others may bring complete sensor systems with data collection capabilities to couple to EMSL automated vapor generation systems. Research areas include sensor arrays, sensor materials design and synthesis, sensing material/analyte interactions, and chemometric methods.

Microfabrication. Microfabrication equipment provides a significant research and development capability in the areas of microstructures, microsensors, and microanalytical systems. Unlike highly automated industrial production equipment, the microfabrication equipment in EMSL has multipurpose functionality. The equipment supports a variety of microprocessing activities that include thin film deposition, various thermal treatments, microphotolithography, chemical etching, inspection and characterization, bonding and packaging, and test and measurement.

Nanobiotechnology Laboratory. The Nanobiotechnology Laboratory is equipped with capabilities to synthesize single-enzyme nanoparticles, functionalize nanostructured matrices, and analyze the activity and stability of enzymes and single-enzyme nanoparticles. This new laboratory consists of various small instruments (such as a black box, a glove box, a Dean Stark system, and shakers), a spectrophotometer, and a spectrofluorometer. A variety of basic enzyme work can be performed in this laboratory including enzyme modification, enzyme immobilization, and enzyme-activity and stability measurements.

Upgrades

Scanning Probe Microscopy Capability Upgrade. There is a great need to establish experimental tools that can acquire single-site chemical information that will lead to important new knowledge in several areas. In particular, heterogeneous catalysis is strongly site specific, and for important catalytic materials such as metal oxides, reactions involve various regular and defect sites. Ideally, one would like to obtain chemically specific information on a sub-nanometer scale. The variable UHV NC AFM/STM purchased in 2004 is ideal for these experiments. We have added many additional surface science capabilities including XPS, AES, and plasma, sputter cleaning, and deposition capabilities.

Liquid Delivery System for MOCVD Capability. EMSL's MOCVD capability is oversubscribed because of demands for instrument time from external users, PNNL programs, and industrial clients. Users of the capability have produced extensive scientific output, including many publications in internationally peer-reviewed journals. Because the MOCVD capability at EMSL has tremendous potential to provide high-quality scientific output, we are upgrading the capability with a new liquid delivery system to repair a failing liquid vaporizer system. At present we are installing and testing the new liquid delivery system with the other MOCVD components. The new liquid delivery system has been tested and demonstrated that high quality films can be generated. Incorporation of this new piece with the main MOCVD system continues.

Heavy Ion Elastic Recoil Detection Analysis Capability. The scientific objective of this project is to develop a high-resolution, TOF-ERDA capability for the EMSL accelerator facility. The TOF-ERDA technique will provide simultaneous detection and absolute quantification of hydrogen, carbon, nitrogen, oxygen, and other light elements as a function of depth in complex matrices containing heavy elements. Because it is a powerful method for investigating elemental concentrations in surface regions, this capability will be effectively applied in many different areas, including characterization of oxide thin films for optical, magnetic, and catalysis applications and characterization of environmental and biological samples, which are primary focus areas at EMSL. Development of this capability will be complete in early 2005.

Enhancement of Deposition capability in the MBE Laboratory. To meet demands, the state-of-the-art oxygen plasma assisted molecular beam epitaxy (OPA-MBE) system was upgraded with additional effusion cells, bringing the total number of individually controlled MBE sources to eight.

Future Directions

The I&NS Facility will continue to focus on innovative research in the areas of surface and interface chemistry, advanced material synthesis and characterization, nanoscience and nanobiotechnology, and catalysis.

More collaborations with scientists from the University of Washington will involve investigations of fundamental science issues that could lead to development of new material systems for thermoelectric power generation. Material synthesis and characterization will be carried out in EMSL thin film deposition and accelerator facilities and surface, and bulk characterization will be carried out in the electron microscopy suite, surface analysis suite, x-ray diffraction facility, and accelerator facility.

Our participation in the Biogeochemistry Grand Challenge will address the scientific issues associated with charge transfer between microorganisms and mineral surfaces. We will approach these issues mainly using our scanning probe capability and electron microscopy.

We also will be a part of the Catalysis Collaborative Access Team involved in the synthesis and characterization of heterogeneous catalysts using methods that provide nanoscale precision in the type, number, and distribution of active sites; the performance and detailed kinetics measurements on model and realistic catalytic systems; the development and testing of new experimental approaches for addressing complex catalysis issues; and the development of new material systems and scientific understanding of mechanisms associated with catalysis.

Adsorption and Reaction of Acetaldehyde on Stoichiometric and Defective $SrTiO_3$(100) Surfaces

L Wang,[(a)] S Azad,[(b)] KM Ferris,[(a)] MH Engelhard,[(b)] and CHF Peden[(a)]
(a) Pacific Northwest National Laboratory, Richland, Washington
(b) W.R. Wiley Environmental Molecular Sciences Laboratory, Richland, Washington

The study of the adsorption and reaction of acetaldehyde on $SrTiO_3$(100) surfaces has provided a fundamental understanding of how surface structures and their defects influence the reactivity. The differences in reactivity between stoichiometric $SrTiO_3$ and TiO_2 surfaces are the result of the unique geometric and electronic structure of the $SrTiO_3$(100) surfaces. New knowledge resulting from this project will lead to improved undertanding of reaction mechanisms in catalysis science.

A fundamental understanding of the decomposition of acetaldehyde on TiO_2 and $SrTiO_3$ surfaces is interesting because of the complexities in the chemistry of aldehydes and the variety of coordination environments provided by these surfaces. As compared with TiO_2(110) and TiO_2(100) surfaces, the TiO_2-terminated $SrTiO_3$(100) surface shows a unique geometric arrangement. The latter surface is rather flat with only in-plane oxygen atoms, whereas the TiO_2(110) and TiO_2(100) surfaces have rows of two-coordinate bridging oxygen atoms lying above the rows of titanium atoms. Adsorption and reactions of acetaldehyde (CH_3CHO) on stoichiometric (TiO_2-terminated) and reduced $SrTiO_3$(100) surfaces have been investigated in this study using temperature-programmed desorption (TPD) and x-ray photoelectron spectroscopy (XPS). Ar^+ ion bombardment is used to systematically shift the average surface oxidation state from Ti^{4+} to Ti^{3+}. Figure 1 displays a narrow and symmetric titanium 2p peak resulting predominantly from Ti^{4+} cations on the oxidized surface, whereas the sputter-reduced surface shows a large broadening in the spin-orbit split titanium 2p peaks caused by the presence of Ti^{3+} and Ti^{2+} cations. Acetaldehyde adsorbs molecularly on the stoichiometric $SrTiO_3$(100) surface that contains predominately Ti^{4+} cations as depicted in Figure 2. The Ti^{4+} sites on the stoichiometric $SrTiO_3$(100) surface are not sufficiently active for

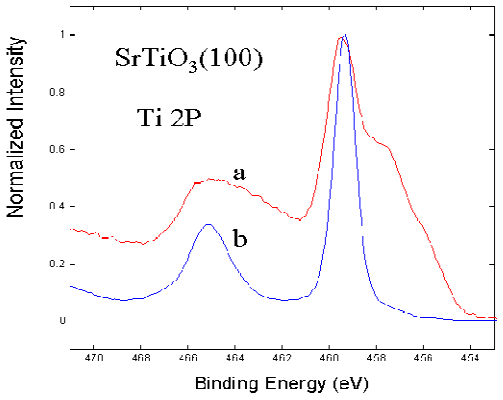

Figure 1. Titanium 2p and oxygen 1s XPS spectra for a sputter-reduced $SrTiO_3$(100) surface a) and a nearly defect-free (stoichiometric) $SrTiO_3$(100) surface b) at 297 K.

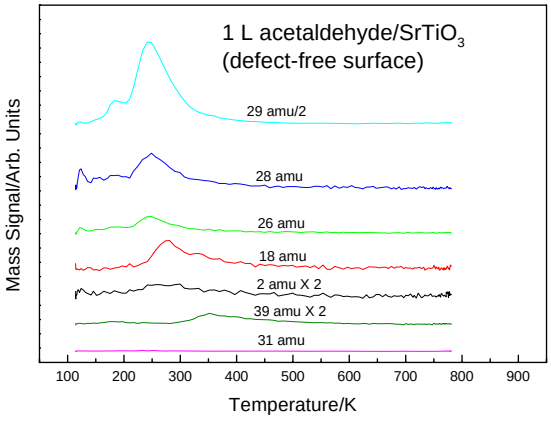

Figure 2. TPD spectra monitoring 2,15,18,26,28,29, and 31 amu, following adsorption of 1 L acetaldehyde on stoichiometric $SrTiO_3$(100) surfaces at 110 K.

reactions such as aldol condensation, as opposed to the Ti^{4+} ions on the TiO_2(001) surface. Aldol condensation, which takes place through the reduction of an oxidized surface, occurs on both {011}- and {114}- faceted TiO_2(001) surfaces containing, four-, five- and six-coordinated cations. The enhanced reactivity of CH_3CHO on the TiO_2(001) surfaces can be attributed to the unique structures of these surfaces that possess a variety of surface sites.

Decomposition and redox reactions of acetaldehyde occur in the presence of surface defects created by Ar^+ sputtering as indicated by the TPD results shown in Figure 3, and the decomposition products include hydrogen (m/e = 2 amu), C_2H_4 (m/e = 28, 27, 26 amu), CO (m/e = 28), C_4H_6 (m/e = 54 amu) and C_4H_8 (m/e = 56 amu). The TPD results clearly indicate that reductive coupling to produce C_2H_4 and C_4H_8 is the main reaction pathway for decomposition of acetaldehyde on the sputter-reduced $SrTiO_3$(100) surface, and equations 1 and 2 illustrate these pathways (here 'g' and 'a' stand for 'gas' and 'adsorbate,' respectively, and Ti^{3+} used here represents reduced cations created by Ar^+ sputtering). Further dehydrogenation of C_4H_8 and formation of butadiene (C_4H_6, m/e 54) is also observed during TPD.

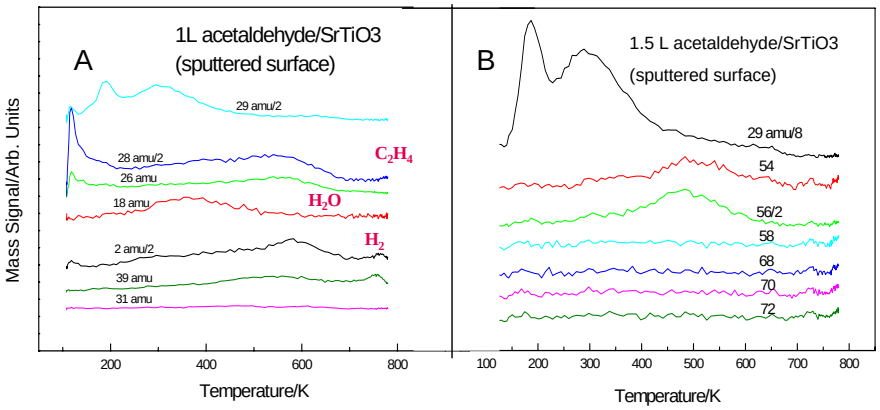

Figure 3. TPD spectra monitoring 2, 15, 18, 26, 28, 29, and 31 amu following adsorption of 1 L acetaldehyde (A) and monitoring 29, 54, 58, 68, 70, and 72 amu following adsorption of 1.5 L acetaldehyde (B) on sputter-reduced $SrTiO_3$(100) surfaces at 120 K.

$$2\ CH_3CHO(a) \rightarrow C_2H_4(g) + 2H_2(a) + 2CO(g) \quad (1)$$

$$2\ CH_3CHO\ (a) \rightarrow C_4H_8(g) + 2O\ (a) \quad (2)$$

$$2\ CH_3CHO\ (a) + 4\ Ti^{3+}(a)+ \rightarrow C_4H_8(g) + 4\ Ti^{4+}(a)+ 2O_2^{-}\ (a) \quad (3)$$

Equation (3) shows that the bimolecular coupling to produce C_4H_8 may also involve the oxidation of Ti^{3+} to Ti^{4+}. The sputter-induced damage is found to be completely healed by annealing during the TPD process, indicating that dissociation of acetaldehyde most likely oxidizes the reduced surface. Similar reductive coupling also takes place on the reduced TiO_2(001) following adsorption of acetaldehyde on these surfaces, suggesting that reduced titanium cation sites are responsible for the initiation of the coupling reactions. The differences in reactivity between stoichiometric $SrTiO_3$ and TiO_2 surfaces presumably originate from the unique geometric and electronic structure of the $SrTiO_3$(100) surfaces.

Anisotropic Thermal Properties of Single-Wall Carbon Nanotube Reinforced Nanoceramics

AK Mukherjee,[(a)] H Wang,[(b)] and CM Wang[(c)]
(a) University of California, Davis, Davis, California
(b) Oak Ridge National Laboratory, Oak Ridge, Tennessee
(c) W.R. Wiley Environmental Molecular Sciences Laboratory, Richland, Washington

Carbon nanotubes are new materials with many potential applications, but a better understanding of their properties is needed. Dispersing carbon nanotubes into another matrix, like a ceramic, may induce unexpected properties. This research highlights the extraordinary thermal conductivity anisotropy of carbon nanotubes-ceramic composites that might be applicable to temperature control.

Anisotropic thermal diffusivity is a quality sought after in materials used in a wide range of applications. This property is typically achieved through the development of porous materials; however, this approach sacrifices other properties such as mechanical strength. Alignment of single-wall carbon nanotubes (SWCNTs) in the matrix by use of high magnetic fields is another way of producing anisotropy in polymer systems. Amiya K. Mukherjee and members of his group at University of California, Davis, are collaborating with Chongmin Wang of W.R. Wiley Environmental Molecular Sciences Laboratory (EMSL) to develop carbon nanotube/alumina composites using EMSL research capabilities. In this study, anisotropic thermal properties have been successfully developed in dense nanocrystalline ceramic composites by incorporating ropes of SWCNTs and using a spark-plasma-sintering consolidation technique (Figure 1). These carbon nanotube/ceramic composites also exhibit improved mechanical properties and metal-like electrical conductivity that would make them possible thermoelectric materials. Such multifunctional carbon nanotube/ceramic composites with novel mechanical, electrical, and anisotropic thermal properties are envisaged for a wide range of applications. Dense SWCNT-reinforced alumina nanocomposites have been fabricated by this novel spark-plasma-sintering technique. Anisotropic thermal properties have been found in carbon nanotube composites (Zahn et al. 2004). The introduction of ropes of SWCNTs gives rise to a decrease of the transverse thermal diffusivity with increasing carbon nanotube content, yet it does not change the in-plane thermal diffusivity.

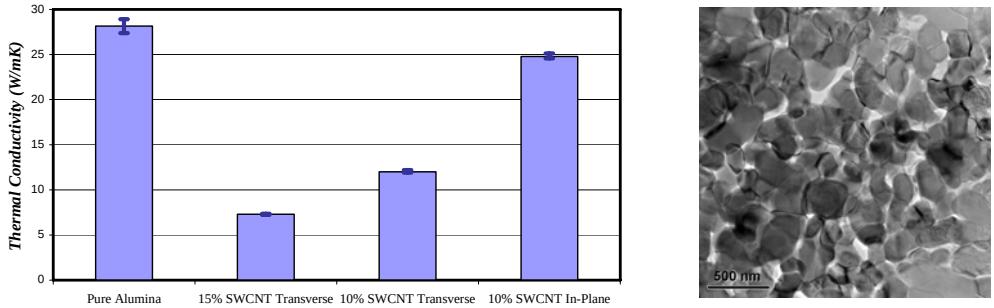

Figure 1. Left: Thermal conductivity with respect to the carbon nanotube content. Right: Transmission electron microscope image showing the microstructure of a carbon nanotube/alumina nanocomposite material.

This finding is scientifically interesting and technologically important for the development of materials for thermal barrier coatings.

Carbon nanotubes are attracting increasing interest as constituents of novel nanostructured materials, sensors, and devices. Rapid advances in bulk synthesis of SWCNTs, coupled with their remarkable mechanical and electrical properties, are positive signs for applications in a host of composite materials. The size, shape, and properties of SWCNTs make them prime candidates for use in the development of potentially revolutionary composite materials. Theory predicts an extremely high value (6600 W/mK) for the room temperature longitudinal thermal conductivity of an individual SWCNT, suggesting that SWCNTs should be ideal for high-performance thermal management. Although this speculation has not yet been demonstrated for SWCNTs, a recent measurement of 3000 W/mK for the room temperature thermal conductivity of an individual multiple-wall carbon nanotube has been reported. However, the experimental measurements of aligned bundles of SWCNTs show a measured thermal conductivity of only 250 W/mK at room temperature and, surprisingly, only 2.3 W/mK for a sintered sample.

Attempts have been made to develop advanced engineering materials with improved or novel properties by taking advantage of the exceptional mechanical properties and the metal-like electrical conduction of carbon nanotubes. It was not until very recently that we successfully demonstrated the potential application of carbon nanotubes as reinforcing agents and electrically conducting fillers in nanoceramic composites. However, no researcher has yet successfully taken advantage of the unique combination of electrical, mechanical, and thermal properties that carbon nanotubes provide in ceramic systems. We show that ropes of SWCNTs successfully confer anisotropic thermal conductivity to nanoceramic materials.

The composites in this study were produced by consolidating the mixture of alumina nanopowders and SWCNTs by spark-plasma sintering. The SWCNTs used in our study were produced by the high-pressure carbon monoxide process and then purified before use to remove the majority of the metallic catalyst particles. SWCNTs tend to self-organize into 'ropes' that consist of many (typically, 10 to 100) tubes running lengthwise in van der Waals bonding with one another. Because of their high surface area and high aspect ratio, the ability to homogeneously disperse the nanotubes in the matrix is a challenge in the processing methods.

Reference

Zahn GD, JD Kuntz, H Wang, CM Wang, and AK Mukherjee. 2004. "Anisotropic Thermal Properties of Single-Wall Carbon Nanotube Reinforced Nanoceramics." *Philosophical Magazine Letters* 84(7):419-423.

Harder Ceramics through Carbon Nanotube Reinforcement

L An[(a)] and CM Wang[(b)]
(a) University of Central Florida, Orlando, Florida
(b) W.R. Wiley Environmental Molecular Sciences Laboratory, Richland, Washington

Brittle fracture is one of the key weaknesses of modern ceramics. Reinforcing ceramics with carbon nanotubes yields a tougher and stronger ceramic. This paper highlights the collaborative research for developing carbon-nanotube-reinforced ceramics.

Carbon nanotubes have attracted tremendous interest in the last decade because of their unusual properties. Theoretical and experimental studies have revealed that carbon nanotubes possess Young's moduli of the order of 1 to 5 TPa and strength as high as 60 GPa (Figure 1). Depending on their diameters and the orientations of their hexagons with respect to the tube axis, nanotubes could be either semiconducting or metallic. The axial thermal conductivity of carbon nanotubes is even higher than that of diamond. These unique properties suggest that carbon nanotubes hold great promise as the basis for new, novel nanocomposites.

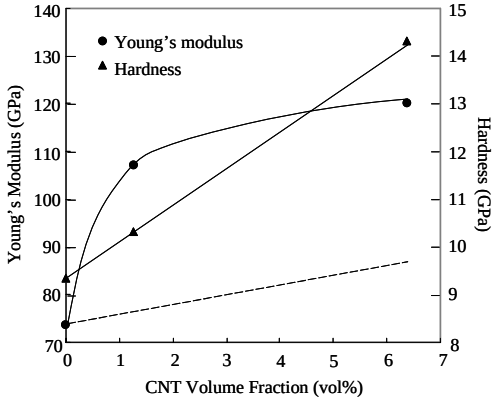

Figure 1. Young's modulus and hardness variation with volume fraction of carbon nanotubes. The dashed line is the theoretical E-modulus calculation. Note that the increase in Young's modulus caused of the presence of carbon nanotubes is much higher than the theoretical prediction.

Carbon-nanotube-reinforced ceramics represent a new class of materials with potential applications for energy, space, and many other industries, including environmental barrier coatings, high-temperature fibers/matrices for composite materials, and extreme environmental micro-electromechanical systems-based sensors. The effective use of carbon nanotubes in ceramic composite applications depends strongly on the capability to disperse the nanotubes homogeneously throughout the matrix, achieve high degree of alignment of the nanotubes, and control the interfacial properties. These requirements are difficult to achieve with conventional powder-based ceramic processing. Previous studies on ceramic/carbon-nanotube composites, in which the samples were prepared by consolidating mixtures of carbon nanotubes and ceramic powders, revealed that only minor improvements in mechanical properties were achieved by adding up to 10 wt% carbon nanotubes.

Linan An of the Advanced Materials Processing and Analysis Center at the University of Central Florida is collaborating with Chongmin Wang of the W.R. Wiley Environmental Molecular Sciences Laboratory (EMSL) to study the mechanical behavior of carbon–nanotube-reinforced ceramics derived from polymer precursors with an end composition of Si-C-N. An, Wang, and their co-workers employed a recently developed polymer-derived-ceramic method to prepare the ceramic/carbon-nanotube nanocomposities (An et al. 2004.)

Unlike conventional ceramics obtained by consolidating respective powders, polymer-derived ceramics are synthesized by direct thermal decomposition of polymer precursors, which could be either liquid, meltable, or dissolvable in other organic solvent. Compared to powder-based processing, this chemical-to-ceramic technique is particularly suitable for fabricating composites containing ceramic/carbon nanotubes (and other reinforcement materials), because the dispersion and alignment of carbon nanotubes can be rather easily achieved in liquid-phase organic forms just prior to pyrolysis.

It is also possible to control the interfacial properties of ceramic/carbon nanotubes by designing the chemistry of the interfaces between the carbon nanotubes and precursors. Carbon-nanotube-reinforced ceramic composites were synthesized using recently developed polymer-derived ceramics as matrices. Multiple-wall carbon nanotubes, treated with a surfactant, were first dispersed in a liquid polymer precursor by sonication and mechanical stirring. The solution then was converted to fully dense ceramic composites with pressure-assist pyrolysis techniques. The carbon-nanotube-reinforced ceramic showed higher hardness and Young's modulus, which is essential for application related to wear resistance and high-strength requirement. Observation of the microstructure of this material revealed that the nanotubes were homogeneously dispersed throughout the ceramic matrix. Significant increases in mechanical and thermal properties were observed by adding only approximately 6 vol% nanotubes. Strong nanotube pullout revealed by scanning electron microscopy observation suggested that the composites could possess high fracture toughness as well.

Reference

An L, W Xu, S Rajagopalan, C Wang, H Wang, Y Fan, L Zhang, D Jiang, J Kapat, L Chow, B Guo, J Liang, and R Vaidyanathan. 2004. "Carbon-Nanotube-Reinforced Polymer-Derived Ceramic Composites." *Advanced Materials* 16(22):2036-2040.

Assembly of Multicomponent Metallic Nanoparticles on Carbon Nanotubes

CJ Zhong,[(a)] CM Wang,[(b)] Y Lin,[(c)] and MH Engelhard[(b)]
(a) University of New York, Binghamton, New York
(b) W.R. Wiley Environmental Molecular Sciences Laboratory, Richland, Washington
(c) Pacific Northwest National Laboratory, Richland, Washington

The ability to modify the surface of carbon nanotubes with a desired functional property is important for exploring applications of carbon nanotubes in sensors and catalysis. This paper highlights recent development on surface modification of carbon nanotubes with metal nanoparticles.

Carbon nanotubes 10 to 50 nm in diameter are fullerene-related graphene cylinders closed at either end with pentagonal rings. The clever C-C organization of the bonds makes them conductive along tubules and quantized across tubules. The unique physical and chemical properties of carbon nanotubes offer unprecedented opportunities for novel applications that are dependent on the electronic conductivity in terms of the diameter and surface properties. Indeed, in the past several years, a variety of potential applications of carbon nanotubes have been demonstrated, including catalysis, sensors, and biosensors. A number of strategies have also been developed for the modification of carbon nanotubes. Recently, end-opened single-wall carbon nanotubes (SWCNTs) have been demonstrated to be solubilized in organic solvents by refluxing in aniline to generate sol-SWCNT, and can be further derivatized by adsorption of hydroxy-stilbene fluorophore onto the carbon surface via ester-coupling. Mixed monolayer-protected gold clusters adsorb strongly onto both end-opened SWCNT and sol-SWCNT. Adsorption of monolayer-protected clusters with hydroxyl groupings in the mixed monolayer onto end-opened SWCNTs occurred without change in shape of the nanotube bundles. Amine-labeled, monolayer-protected clusters were less aggressive adsorbers. In recent years, carbon nanotubes have stimulated extensive research into the properties of nanometer-scale networks and catalysis for hydrogen storage materials and in fuel cells. Filling metal nanoparticles inside template (alumina membranes)-synthesized carbon nanotubes has been elegantly demonstrated for methanol oxidation and oxygen reduction.

In most of the modification strategies, different surface coupling chemistries have been exploited for the surface functionalization of carbon nanotubes. While these strategies are effective, controllability has not been fully realized. In view of the high surface area of carbon nanotubes and the associated high surface activity, it has been realized that the direct assembly of monolayer-capped metal nanoparticles outside carbon nanotubes should be possible. Monolayer-capped nanoparticles are known to have well-defined interparticle spatial properties. By assembling such nanoparticles onto carbon nanotubes, it would be expected that the aggregation or clustering for the carbon nanotubes could be reduced, and the accessibility to the nanoparticle and carbon nanotube surfaces could be increased because of the high rigidity of the carbon nanotubes. Because the surface of carbon nanotubes can be functionalized (e.g., treatment with HNO_3 to produce surface -CO_2H groups) to manipulate the surface anchoring ability or surface free energy, we also expect to

gain additional controllability over particle-substrate adhesions, which are important for many practical sensor and catalysis applications.

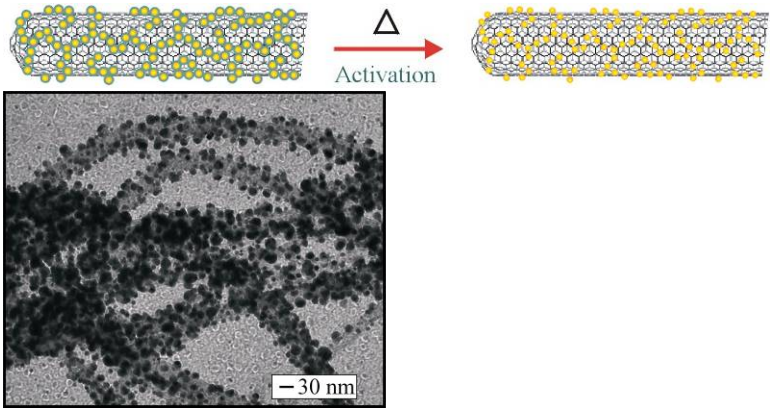

Figure 1. Top: Schematic illustration of thermal treatment leading to removal of the capping agent from the capped nanoparticles supported on a carbon nanotube. Bottom: Transmission electron micrograph of carbon nanotube-supported gold nanoparticles.

The ability to modify the surface of carbon nanotubes with the desired functional properties is important for exploring applications in sensors and catalysis. We have developed a chemical method, based on an exchange-crosslinking-precipitation strategy, for dressing single or multicomponent metallic nanoclusters on carbon nanotubes. Typically, with this approach, gold nanoparticles of 2- to 5-nm core sizes can be dressed onto carbon nanotubes with controllable loading and interparticle spatial properties. Both ordered and disordered morphologies of the assembled nanoparticles have been revealed. We have demonstrated (Figure 1) the assembly of monolayer-protected gold nanoparticles on multiple wall carbon nanotubes by a simple and effective route. Assemblies of gold nanoparticles of 2- to 5-nm core sizes onto carbon nanotubes have displayed both ordered and disordered morphologies of the assembled nanoparticles. By thermal removal of the shell structure of the assembled nanoparticles, the size and interparticle spatial properties were demonstrated to be dependent on the initial loading of the nanoparticles. Further investigations using the nanoparticles/carbon nanotubes nanocomposited for the fabrication of nanostructured biosensors and high-efficiency fuel cells are in progress. This collaborative research has resulted in two peer reviewed publications (Han et al. 2004; Kariuki et al. 2004) and several presentations.

References

Han L, W Wu, FL Kirk, J Luo, MM Maye, NN Kariuki, Y Lin, C Wang, and CJ Zhong. 2004. "A Direct Route Toward Assembly of Nanoparticle-Carbon Nanotube Composite Particles." *Langmuir* 20(14):6019-6025.

Kariuki NN, J Luo, MM Maye, SA Hassan, T Menard, HR Naslund, Y Lin, C Wang, ME Engelhard, and CJ Zhong. 2004. "Composition-Controlled Synthesis of Bimetallic Gold-Silver Nanoparticles." *Langmuir* 20(25):11240-11246.

Dissolution and Growth of (10$\bar{1}$4) Calcite in Flowing Water: Estimation of Back Reaction Rates Via Kinetic Monte Carlo Simulations

RE Williford,[(a)] DR Baer,[(a)] JE Amonette,[(a)] and AS Lea[(b)]
(a) Pacific Northwest National Laboratory, Richland, Washington
(b) W.R. Wiley Environmental Molecular Sciences Laboratory, Richland, Washington

Calcite, or calcium carbonate, is found in various forms throughout the world. The dissolution and growth of carbonates have environmental impacts that include the global carbon cycle, and attempts are being made to design carbon dioxide sequestration systems to control global warming and contaminant transport in groundwater. Understanding the molecular details of growth and dissolution will help predict contaminant spread or containment in groundwater and will contribute to solutions in environmental remediation and the design of carbon sequestration systems.

Although calcite is an important mineral for many processes, there have been relatively few simulations of its growth and dissolution behavior. Such simulations are complicated by the multitude of defect types and by the asymmetry of the crystal. Recently, work combining a kinetic Monte Carlo model involving a modified cubic crystal structure and a Blasius liquid boundary layer was used to simulate the simultaneous growth and dissolution reactions on the calcite cleavage surface in flowing water. Using the atomic force microscope (AFM) in the W.R. Wiley Environmental Molecular Sciences Laboratory (EMSL), the model was developed as part of a U.S. Department of Energy Geosciences program to help understand the impact of solution flow on measurements made of pit growth. The activation energies of the back reaction (growth) were determined from those of the forward reaction (dissolution) by obtaining agreement with cleavage-step morphologies and step dissolution velocities over a range of flow rates measured using the AFM. Because the model includes the elemental reaction steps, information about the occurrence of specific steps influencing an overall reaction rate can be estimated. The kinetics of dissolution and growth were found to be dominated by diffusion events on the solid/liquid interface and in the liquid, as expected. One of the experimental observations involves changes in the shape of steps as solution flow changes. The differences between a relatively smooth dissolution step at rapid solution flow and a rougher step for slower solution flow can be seen in Figure 1. The relative magnitudes of desorption and adsorption activation energies were consistent with experimental data, entropic arguments, and crystal roughening theories. Because all of the boundary layer parameters cannot be determined from first principles, there is one adjustable parameter involved in fitting the data. However, quantitative agreement with

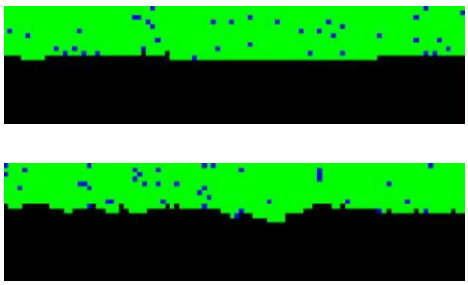

Figure 1. Example of steady-state step face geometry calculated by the kinetic Monte Carlo method at high flow rate (top) and at low flow rate (bottom).

measured step velocities is best when the boundary layer parameters were given physically reasonable values, as shown in Figure 2.

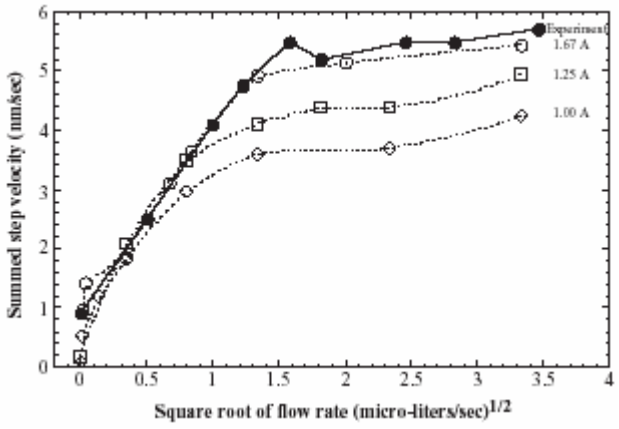

Figure 2. Sum of step velocities versus the square root of the fluid flow rate. Numbers indicate multipliers for the entropic prefactors (AD and AA).

In addition to those mentioned above, the results of the simulations exhibit several interesting features. The simulated step morphologies are in good qualitative agreement with superparamagnetic images over the full range of flow rates. Events at the step face are dominated by surface diffusion (approximately 70%), as expected. Desorption and adsorption account for about approximately 15% each. The approach to equilibrium is rapid because of the small size of the liquid region in the model. A larger liquid region simply required more cycles to reach equilibrium, but results were within the scatter inherent in the kinetic Monte Carlo method. Activation energies for adsorption (growth) were found to be less than those for desorption (dissolution). This finding is consistent with crystal roughening theories and with experiments on bulk calcite. Several authors have explored the phenomenon of 'kinetic asymmetry' associated with crystal roughening theories. For smooth surfaces, it is found that growth rates are generally faster than dissolution rates, which agrees with rate constants computed from the present simulations. The situation is reversed for rough surfaces, especially at the corners of growth islands. The Blasius boundary layer approximation appears adequate for simulation of calcite dissolution and growth under flowing fluid conditions in the AFM wet cell. The flow constant corresponds to a boundary layer development length of 7.8 Å. This is physically reasonable because it indicates that the boundary layer is developing within a few lattice constants for the given flow conditions. It is also in agreement with previously reported 5.3 Å thick 'organized water layer' on calcite surfaces. Thus, the model appears self-consistent.

The Effect of Water on the Adsorption of NO_2 in Sodium- and Barium-Yttrium, Faujasite Zeolites: A Combined Fourier Transform Infrared and Temperature-Programmed Desorption Investigation

JH Kwak,[(a)] J Szanyi, [(b)] and CHF Peden[(b)]

(a) W.R. Wiley Environmental Molecular Sciences Laboratory, Richland, Washington
(b) Pacific Northwest National Laboratory, Richland, Washington

The effect of water on the overall NO_x reduction activities of zeolite-based catalysts has long been recognized. We investigated how the presence of water influences the adsorption of NO_2 on sodium- and barium-yttrium faujasite zeolites active in the non-thermal plasma assisted catalytic NO_x reduction. A better understanding of this may lead to potential solutions for the reduction of atmospheric pollution.

The removal of NO_x from automotive exhaust gases is a tremendous challenge to the developers of catalytic converters, in particular when the engine is operated under lean conditions (i.e., in excess-oxygen conditions as occurs with diesel engines). Under these conditions, the traditional three-way catalysts do not work because of their very high hydrocarbon oxidation activity, which depletes the reducing agent before NO_x reduction occurs. Among the most promising new technologies for diesel exhaust aftertreatment are the NO_x adsorber and non-thermal plasma assisted catalytic NO_x reduction. Base metal oxide adsorbers (in particular BaO) have been shown to be highly effective for the removal of NO_x from an oxygen-rich exhaust gas mixture. Recently, we reported very promising activities for both sodium- and barium-yttrium, faujasite (FAU) zeolites in catalytic lean NO_x reduction when the catalyst was used in conjunction with non-thermal plasma. The two most important reactions that take place in the plasma are the almost complete conversion of NO to NO_2 and the formation of partially oxidized hydrocarbon species (acetaldehyde [CH_3CHO]) in significant quantities. Combining the strong oxidizing power of NO_2 and the ease of oxidizability of CH_3CHO results in high levels of NO_x reduction over these base zeolite catalysts at relatively low temperatures (approximately 473 K).

We have reported previously that exchanging the charge compensating Na^+ ions for Ba^{2+} ions in yttrium, faujasite (FAU) zeolites increases the NO_x conversion by more than 10%, and also widens the temperature window in which high activity can be sustained. We have suggested that one possible explanation of this activity enhancement was the stronger adsorption of NO_2 observed over barium-yttrium in comparison to sodium-yttrium. Here we report on our recent finding on the adsorption of NO_2 on both sodium- and barium-yttrium. We used Fourier transform infrared spectroscopy to identify the nature of adsorbed species, and correlated those finding with results obtained from temperature-programmed desorption of NO_2. The adsorption and desorption of NO_2 were investigated on both water-free (dry) and water-containing (wet) catalysts.

The interaction of NO_2 with both sodium- and barium-yttrium, FAU zeolites resulted in the formation of the same type of ionic species. In the absence of adsorbed water, NO^+ ions formed by the disproportionation of NO_2 are adsorbed onto framework O- sites associated

with the charge compensating cationic positions of the zeolite, while NO_3^- ions are bound to the charge compensating cations. At high NO_2 dosages, NO^+NO_2 adducts can form on both catalysts. The thermal stabilities of these adsorbed NO_x species strongly depend on the nature of the charge compensating cation. The adsorption of these species is much weaker over sodium-yttrium as a large fraction of the NO^+ and NO_3^- desorb even upon evacuation at 295 K. On the other hand, all the adsorbed NO_x species are much more stable over barium-yttrium, so much so that even most of the NO^+NO_2 species are present on this catalyst following room-temperature evacuation. The presence of water dramatically influences the adsorption of NO_2 on both materials, as it competes for the available adsorption sites and also reacts with some of the adsorbed NO_x species. The number of adsorbed NO^+ species decreases with increasing amounts of water added, and HNO_x species are formed that, by interacting with the charge compensating cations, form zeolitic-O-H groups and $M^{n+}(NO_x)_n$. The NO_2 temperature-programmed desorption feature in sodium-yttrium shifts from 350 K to 520 K, while on barium-yttrium, the corresponding temperature-programmed desorption feature shifts from 470 K to 670 K. The effect of water on the adsorption of NO_2 on barium-yttrium is shown in Figure 1. The series of temperature-programmed desorption spectra were obtained at a constant level of NO_2 dosing while varying the amount of water pre-adsorbed onto the barium-yttruim sample. The series infrared spectra were recorded by gradually increasing the amount of water added to an NO_2, ads.-barium-yttrium sample. The large differences found here in the stabilities of adsorbed NO_x species over these two catalysts seem to strongly correlate with their vastly different catalytic activities observed in the non-thermal plasma assisted NO_x reduction.

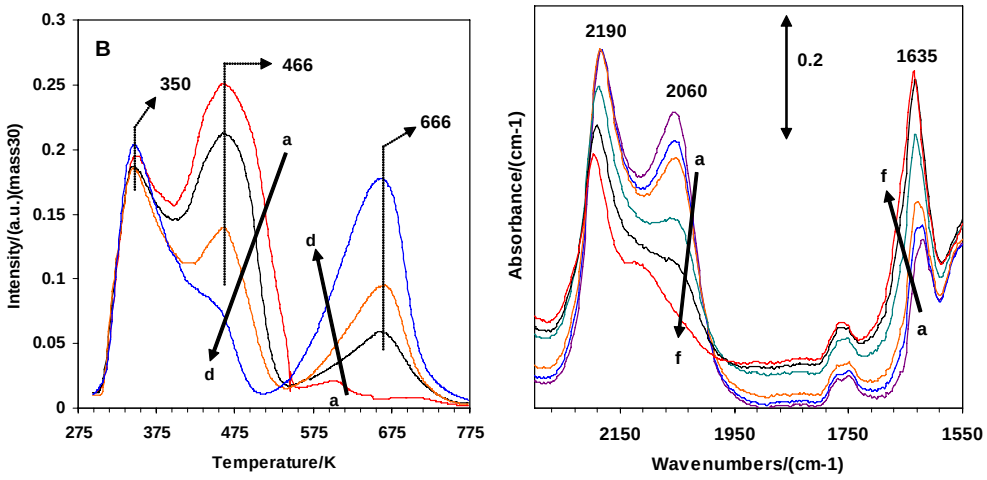

Figure 1. The effect of water on the adsorption of NO_2 over barium-yttrium.

Influence of GaN Template Layer Strain on the Performance of InGaN/GaN Multilayer Quantum Well Light-Emitting Diodes

MC Johnson,[(a)] ED Bourret-Courchesne,[(a)] J Wu,[(a)] Z Liliental-Weber,[(a)]
DN Zakharov,[(a)] RJ Jorgenson,[(b)] TB Ng,[(b)] DE McCready,[(c)] and JR Williams[(d)]
(a) Lawrence Berkeley National Laboratory, Berkeley, California
(b) Oriol, Incorporated, Santa Clara, California
(c) W.R. Wiley Environmental Molecular Sciences Laboratory, Richland, Washington
(d) Pacific Northwest National Laboratory, Richland, Washington

Group-III nitrides such as GaN have become extremely important as light emitting diodes and high-power laser diodes used everyday in electronic devices. Because of the difficulties associated with bulk systems of these materials, they are synthesized in thin film form on various substances. This highlight describes the growth and characterization of InGaN/GaN multi-layer thin films using metal organic chemical vapor deposition.

Group-III nitrides have become extremely important in device applications over the last decade. High-brightness light-emitting diodes (LED) and high-power laser diodes (LD) based on these materials are already commercially available. Because of excess dissociation pressure at the high temperatures necessary for crystal growth, Group-III nitrides cannot be economically fabricated in bulk single-crystal form. As such, these materials must be deposited heteroepitaxially on a foreign substrate. For example, InGaN/GaN multi-layer quantum well (MQW) structures are typically grown on a GaN template layer deposited on a sapphire substrate. However, GaN has large lattice and thermal expansion coefficient mismatches with sapphire, approximately 32% and 56%, respectively. The resulting strain and defect formation in the GaN template can affect the properties of the overlaying MQW structure.

In this study, we examined the effects of template strain on the performance of two seven-period InGaN/GaN MQW LEDs grown by metallorganic chemical vapor deposition (MOCVD). Except for the thickness of the GaN template layers (5 μm and 15 μm, respectively), the deposition parameters were identical. Figure 1 shows that the electroluminescence emission of the device grown on the 15-μm template was red-shifted by approximately 132 meV. An overlay plot of the triple-axis, x-ray diffraction (TAXRD) rocking curves for both LEDs is shown in Figure 2. The many well-resolved satellite peaks

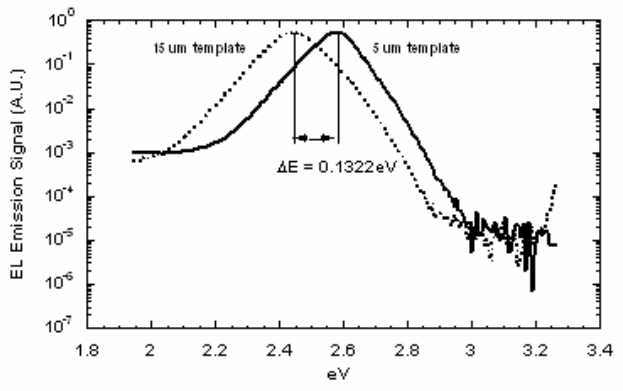

Figure 1. Electroluminescence emission for InGaN/GaN MQW devices grown simultaneously on 5-μm and 15-μm GaN templates. The output of the device on the 15-μm template is red-shifted by approximately 132 meV.

showed that these were high-quality films, while the position of the GaN (002) peak indicated that the perpendicular strain was +0.04% in the 5-µm template and -0.002% in the 15-µm template. Although not illustrated here, the position of the asymmetric GaN (105) peak for these films indicated that the parallel strain was -0.10% in the 5-µm template and +0.009% in the 15-µm template. These results indicate there was less residual strain in the thicker template. Cross-section transmission electron microscopy images of both devices are shown in Figure 3.

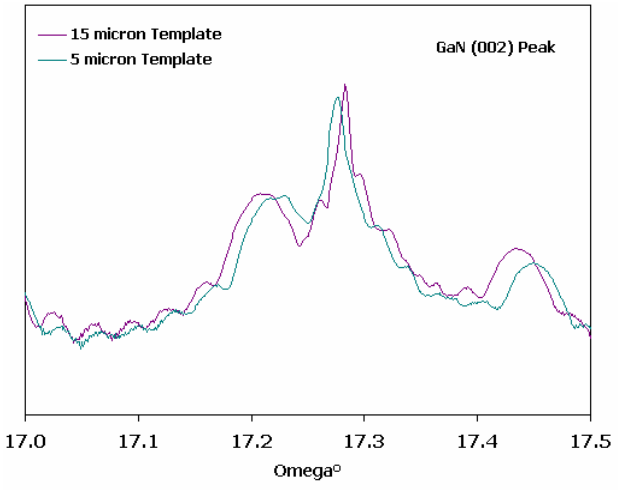

Figure 2. Expanded scale overlay plot of the TAXRD rocking curves for both devices.

These images verified the thickness of the template layers. In addition, the edge dislocation density was 0.4 x 10^8/cm^2 in the 5-µm template and 1.9 x 10^8/cm^2 in the 15-µm template. Note that the higher dislocation density in the thicker template was consistent with the strain relaxation observed by TAXRD. Depth profiling by dynamic secondary ion mass spectroscopy was also performed to obtain the indium concentration in the active region of these devices. On a relative scale, the average indium concentration was approximately 11% higher for the device grown on the 15-µm template. This difference in indium concentration was attributed to strain-induced thermodynamic effects that influenced the MQW growth and ultimately caused the red-shift illustrated in Figure 1. These results showed the importance of template strain in the design and fabrication of InGaN/GaN MQW LEDs.

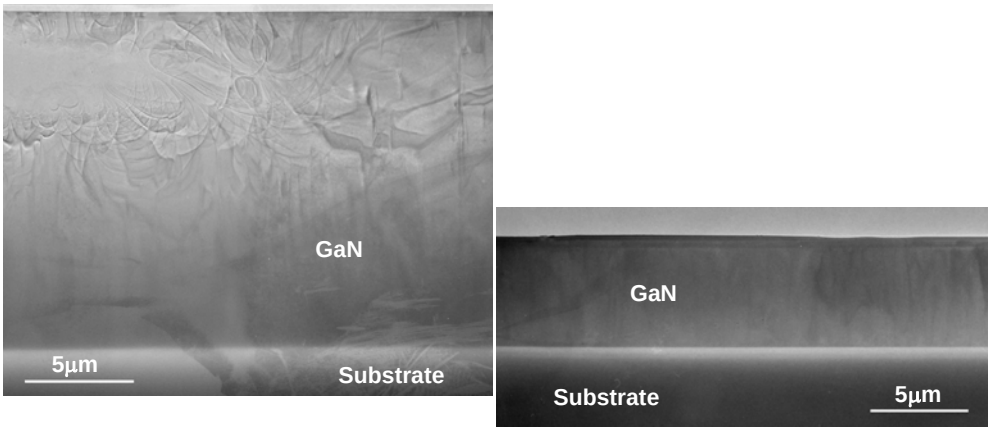

Figure 3. Cross-section transmission electron microscope images of both devices showing the differences in template layer thickness and dislocation density. The edge dislocation density was 0.4 x 10^8/cm^2 in the 5-µm template and 1.9 x 10^8/cm^2 in the 15-µm template.

Interaction of Water with Ordered Alumina Ultra-Thin Films Grown on NiAl(100)

E Ozensoy,[(a)] J Szanyi,[(a)] and CHF Peden[(a)]
(a) Pacific Northwest National Laboratory, Richland, Washington

Metal oxide surfaces have been extensively studied for their relevance to a vast number of material-engineering and catalytic-process applications and for potential solutions to atmospheric pollution. In particular, alumina polymorphs have been the catalytic support of choice for various profoundly important catalytic processes. Water adsorption on solid metal oxide surfaces is a key step in these catalytic systems in which the nature of the interaction between water and the metal oxide surface, as well as its interaction with other reactants, dictate the fundamental reactivity and selectivity trends.

Water adsorption on metals and metal oxide surfaces has been thoroughly discussed in the literature (Henderson 2002). According to these reports, there is a strong interaction between the adsorbed water species and oxide surfaces. Commonly, at relatively low coverages, water is found to adsorb molecularly on the cation sites of the oxide surface, leading to isolated water molecules that lack intermolecular hydrogen bonding. The typical adsorption configuration of water to the oxide surface under these conditions involves bonding between the Lewis acid sites of the oxide (i.e., cationic sites) and the lone pair of the O atom in the water molecule. As the coverage of adsorbed water is increased, formation of hydrogen bonds interlinking originally isolated water molecules are observed, which eventually results in crystalline or amorphous multilayer ice formation. The nature of water adsorption (i.e., molecular or dissociative) on alumina surfaces seems to be closely related to the structure. Although water was reported to adsorb molecularly on ordered γ-Al_2O_3/NiAl(110) thin films (Tzvetkov et al. 2003), it was found to adsorb dissociatively on Al_2O_3/Al(111) (Chin et al. 1986), α-Al_2O_3(0001) (Coustet and Jupille 1994), and γ-Al_2O_3/NiAl(100) (Ivey et al. 2003).

In this study, we focus on the properties of ordered θ-Al_2O_3 ultra-thin films grown on a NiAl(100) single crystal substrate with stoichiometry, morphology, and chemical structure that can be analyzed in detail with conventional surface analysis probes (x-ray photoelectron spectroscopy, Auger electron spectroscopy, temperature-programmed desorption, and low-energy electron diffraction). Therefore, the nature of the interaction between θ-Al_2O_3 polymorphs with adsorbed water can be thoroughly investigated, and related to the structural properties of the alumina thin films.

Our results are summarized as follows:

- Water adsorption on the θ-Al_2O_3/NiAl(100) surface is predominantly molecular rather than dissociative.
- For θ_{H2O} less than 1 ML, water molecules populate Al^{3+} cation sites (Figure 1, right panel) to form isolated water species ordered in rows along the cation sites of the oxide surface. Repulsive interactions between these adsorbed water molecules are indicated by a significant reduction in the desorption temperature with increasing water coverages up to 1 ML.

- For θ_{H2O} greater than 1 ML, water overlayers were observed to form three-dimensional ice multilayers. Water molecules occupy both cationic and anionic adsorption sites on the oxide surface allowing the formation of hydrogen bonding in the ice network.
- A small extent of water dissociation attributed to the presence of a low concentration of surface defects was observed to occur on the θ-Al_2O_3/NiAl(100) surface. Titration of the defect sites with adsorbed water molecules revealed a defect density of approximately 0.05 ML for the θ-Al_2O_3/NiAl(100) system, which is consistent with the highly ordered nature of the oxide film suggested by the low-energy electron diffraction images (Figure 1, left panel).

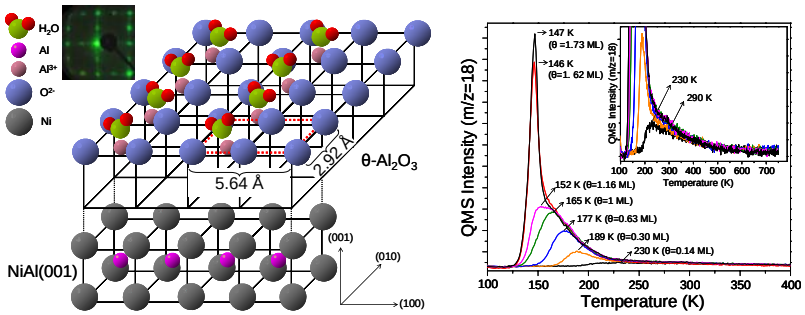

Figure 1. Left panel: Schematic illustrating the θ-Al_2O_3/NiAl(100) surface structure and the water adsorption on the oxide film at $\theta_{H2O} \leq 1$ ML. Right panel: Temperature programmed desorption results for water overlayers on θ-Al_2O_3/NiAl(100) model catalyst.

References

Chen JG, JE Crowell, and JT Yates Jr. 1986. "Assignment of a Surface Vibrational Mode by Chemical Means: Modification of the Lattice Modes of Al_2O_3 by a Surface-Reaction with H_2O." *Journal of Chemical Physics* 84(10):5906-5909.

Coustet V and J Jupille. 1994. "High-Resolution Electron-Energy-Loss Spectroscopy of Isolated Hydroxyl-Groups on χ-Al_20_3(0001)." *Surface Science B* 307-309:1161-1165.

Henderson MA. 2002. "The Interaction of Water with Solid Surfaces: Fundamental Aspects Revisited." *Surface Science Reports* 46(1-8):1-308.

Ivey MM, KA Layman, A Avoyan, HC Allen, and JC Hemminger. 2003. "Characterization of Ultra-Thin Films of χ-Al_20_3 and the Chemistry of 1,3-Butadiene on NiAl(001) and χ-Al_20_3." *Journal of Physical Chemistry B* 107(26):6391-6400.

Tzvetkov G, Y Zubavichus, G Koller, T Schmidt, C Heske, E Umbach, M Grunze, MG Ramsey, and FP Netzer. 2003. "Growth of H_2O Layers on an Ultra-Thin Al_2O_3 Film: From Monomeric Species to Ice." *Surface Science* 543(1-3):131-140.

Intrinsic High-Temperature Ferromagnetism in Chromium-Doped TiO_2 Anatase

TC Droubay,[(a)] J Osterwalder,[(b)] TC Kaspar,[(a)] SM Heald,[(a)] and SA Chambers[(a)]
(a) Pacific Northwest National Laboratory, Richland, Washington
(b) University of Zürich, Zürich, Switzerland

In the emerging field of magneto-electronic devices, spintronics uses both the spin and the charge of the electron. A single material that combines both magnetic and semiconducting behavior will enable straightforward integration of magnetic components into the existing semiconductor framework. In addition to the technological interest, the study of ferromagnetic semiconductors is revealing new and intriguing physical properties as yet unexplained by current theory.

Since their initial discovery in 2001, magnetically doped oxide films that exhibit ferromagnetism at and above room temperature, such as cobalt-doped TiO_2 anatase ($Co_xTi_{1-x}O_2$), have been controversial. Although early investigations of cobalt-doped TiO_2 grown by oxygen plasma-assisted molecular beam epitaxy (OPA-MBE) revealed cobalt (II) substitution for titanium (IV) in the anatase lattice, other studies involving pulsed laser deposition as the growth method produced embedded cobalt metal particles, leading to skepticism as to whether $Co_xTi_{1-x}O_2$ could exhibit intrinsic ferromagnetism. In this paper, we show that TiO_2 anatase doped with chromium, an antiferromagnetic metal, exhibits intrinsic ferromagnetism up to 690 K. Evidence suggests that the intrinsic ferromagnetism in this material grown by molecular beam epitaxy is plausible in comparing chromium-doped TiO_2 in the anatase and rutile polymorphs.

Chromium-doped TiO_2 anatase and rutile films were grown by oxygen plasma-assisted molecular beam epitaxy on $LaAlO_3$(001) and TiO_2(110), respectively. The doping level (x in $Cr_xTi_{1-x}O_2$) was varied between approximately 0.02 and 0.20 with a degradation in crystallinity occurring above approximately x~0.13 in anatase. Chromium (III) substitutes for titanium (IV) in both host lattices over the full range of chromium concentrations were investigated. The films are highly resistive (r greater than approximately 4 KΩ-cm) as grown, but can be made more conductive by annealing in ultra-high vacuum.

Semi-insulating chromium-doped anatase exhibits room-temperature ferromagnetism for all dopant concentrations investigated, whereas chromium-doped rutile does not exhibit ferromagnetism at any concentration. Typical hysteresis loops for as-grown chromium-doped anatase and rutile are shown in Figures 1 and 2, respectively.

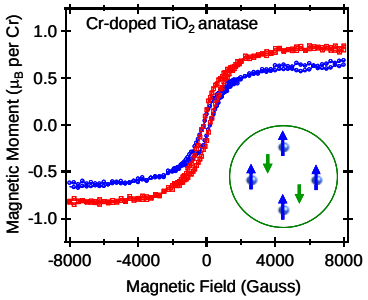

Figure 1. Magnetic properties of 260 Å $Cr_{0.1}Ti_{0.9}O_{1.95}$/315 Å TiO_2 anatase/$LaAlO_3$(001). Vibrating sample magnetometry hysteresis loops taken at room temperature with the magnetic field in the plane of the film for the semiinsulating state (blue) and in the semiconducting state (red). A structural diagram depicting the magnetic coupling of F center electrons and Cr spins is depicted in the lower right. The substrate dimensions were 10 mm x 10 mm x 1 mm. M_s was measured parallel to the side of the square.

Chromium-doped anatase is clearly ferromagnetic, with a saturation magnetization M_s of approximately 0.6 μB/chromium atom, a remanence of approximately 18%, and a coercive field of approximately 180 Gauss. In contrast, chromium-doped rutile is essentially nonmagnetic. The magnetization changes in both anatase and rutile polymorphs as a result of carrier introduction by vacuum reduction.

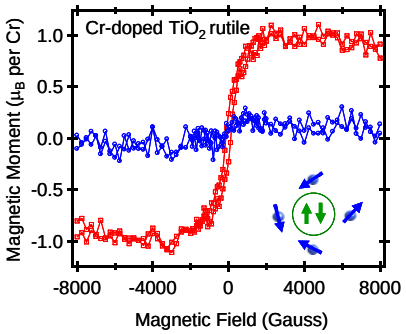

Figure 2. Same as Figure 1, except for 300 Å $Cr_{0.02}Ti_{0.98}O_2$ rutile/TiO_2(110) rutile.

The red curves in Figures 1 and 2 correspond to films made semiconducting at room temperature by thermal reduction in ultrahigh vacuum at approximately 600°C. In chromium-doped anatase, the saturation moment increases from approximately 0.6 μB/chromium atom to approximately 0.8 μB/chromium atom. Rutile goes from being nonmagnetic to ferromagnetic with a saturation moment of approximately 1.0 μB/chromium atom. Upon reduction, the chromium-doped rutile crystal changed from being colorless to a navy blue color, while no color change was evident in the anatase crystal.

The temperature dependence of saturation magnetization moment for chromium-doped anatase obtained in the zero-field cooled and field-cooled magnetizations is shown in Figure 3. The intrinsic ferromagnetism seen in chromium-doped anatase persists well above room temperature to a Curie point (T_C) of 690 K. Chromium K-shell near-edge x-ray absorption spectroscopy and extended x-ray absorption fine structure spectroscopy show that chromium remains in the +3 charge state and at titanium lattice sites. Moreover, the film remains highly resistive at room temperature. We propose that two distinct mechanisms for ferromagnetism are operative in these materials. For semi-insulating $Cr_xTi_{1-x}O_2$, we argue that F-center (or bound magnetic polaron) formation plays a crucial role. To maintain charge neutrality, one oxygen vacancy for every two chromium atoms may be introduced. Applying a simple Bohr model, the orbital radius available for electrons in anatase is approximately 16 Å compared to approximately 2 Å in rutile, owing to the differences in static dielectric constant and effective mass for conduction electrons. The larger sphere of influence for the vacancies explains the differences observed in the magnetic response in the as-grown semi-insulating states of the chromium-doped TiO_2 polymorphs, anatase and rutile. Carrier exchange, the second mechanism, becomes operative when $Cr_xTi_{1-x}O_2$ in either of the polymorphs is made semiconducting via reduction. Itinerant electrons are expected to ferromagnetically couple the dopant spins in the same way as do holes in manganese-doped GaAs. The introduction of free carriers enhances the ferromagnetism in anatase, and creates ferromagnetism in rutile.

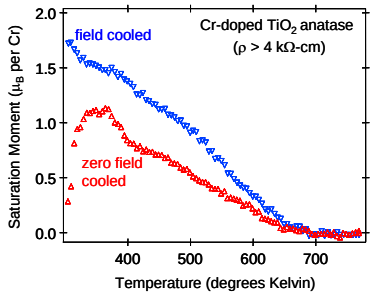

Figure 3. Determination of Curie point for chromium-doped TiO_2 anatase. M_s for 630 Å $Cr_{0.1}Ti_{0.9}O_{1.95}$ (001) anatase vs. temperature in the zero-field cooled (red) and field-cooled (blue) modes. The sample dimensions were 10 mm x 5 mm x 1 mm, and M_s was measured parallel to the short in-plane direction because of space constraints in the vibrating sample magnetometer oven. This material exhibits strong shape anisotropy. Thus, the value of M_s along the short in-plane direction is less than that seen in Figure 1.

Investigation of Chromium as an Alternative Adhesion Layer in Platinum/Silicon Electrodes for Ferroelectric Perovskites

TC Kaspar,[a,b] CL Aardahl,[a] DE McCready,[c] AS Lea,[c] BR Johnson,[a] DW Matson,[a] TS Dory,[d] and JW Rogers, Jr.[c]

(a) Pacific Northwest National Laboratory, Richland, Washington
(b) University of Washington, Seattle, Washington
(c) W.R. Wiley Environmental Molecular Sciences Laboratory, Richland, Washington
(d) Intel Corporation, Chandler, Arizona

The deposition of thin-film perovskites on conducting electrodes is technologically relevant for microelectronics applications. The crystalline quality, and thus the desired device properties, of thin-film perovskites can be greatly enhanced by improvements to the bottom conducting electrode material.

The deposition of thin-film perovskites such as (Ba,Sr)TiO_3 and lead(Zr,Ti)O_3 on conducting electrodes is technologically relevant for microelectronic applications, such as dynamic random access memory (DRAM) and non-volatile ferroelectric random access memory (FRAM). Platinum is often chosen as the bottom electrode material because of its oxidation resistance during subsequent perovskite film deposition. When polycrystalline platinum thin films are deposited on silicon (001) or SiO_2/silicon (001), it is necessary to include a thin layer of another material at the interface to improve the platinum adhesion. Titanium is the most common adhesion layer, although TiO_2, tantalum, ZrO_2, and TiN have also been investigated. Because these adhesion materials are not lattice-matched to platinum, the resulting platinum film is polycrystalline with a strong (111) orientation. It is desirable to deposit perovskites with (100) orientation, and a close lattice match exists between plantinum (100) and both (Ba,Sr)TiO_3(100) and Pb(Zr,Ti)O_3(100). In this study, to enhance the formation of platinum (100) during sputter deposition, chromium was explored as an alternative adhesion layer because of the close lattice match between chromium (100) and platinum (100). We found that cubic chromium nucleated and stabilized platinum (100) in addition to the low-energy surface platinum (111), to a thickness of 40 to 60 nm. Beyond this critical thickness, platinum (111) dominated the growth. Thin platinum films (42 nm) could be deposited with a significant fraction of platinum (100), as observed by x-ray diffraction (Figure 1). The behavior of the platinum/chromium/silicon electrode structure at elevated temperatures in an oxygen ambient is important for perovskite film deposition. The platinum surface was found to form hillocks after thermal cycling as a stress relief mechanism. In addition, Auger electron spectroscopy depth profiling of films processed under ferroelectric conditions indicated chromium diffused into the platinum film, resulting in a thick CrO_x layer on the platinum surface (Figure 2). This thermal instability makes chromium an unsuitable adhesion layer for platinum electrodes.

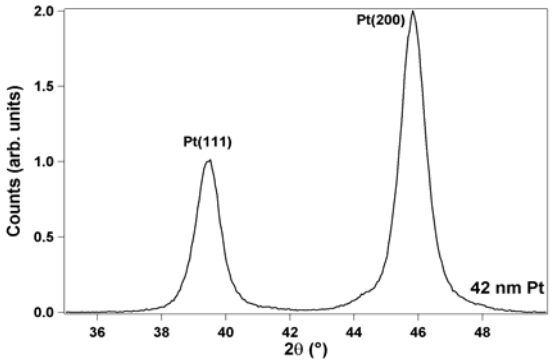

Figure 1. X-ray diffraction pattern of 42-nm platinum/30-nm chromium/silicon (001). After background subtraction, the pattern was normalized to the platinum (111) peak height. A significant proportion of platinum (100) can be realized with a chromium adhesion layer.

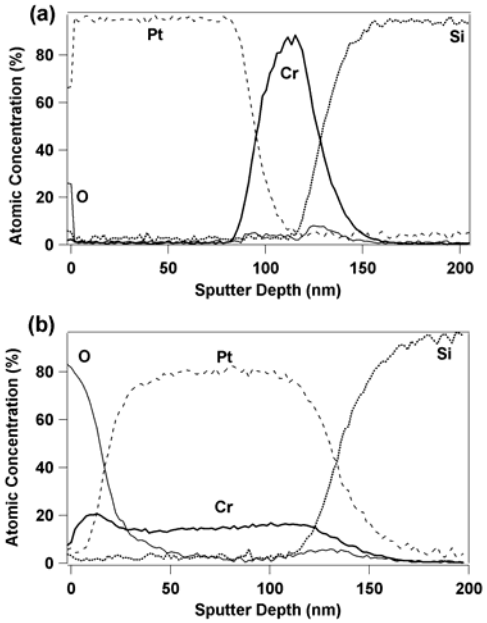

Figure 2. Auger electron spectroscopy depth profiles of 50 nm platinum/30-nm chromium/silicon (001), given as atomic concentration. (a) As-deposited electrode structure. No diffusion is observed. (b) After annealing at 530°C for 60 minutes in 80 sccm O_2. Chromium diffusion into the platinum film is observed, as well as a thick layer of CrO_x at the platinum surface.

Lateral Ordering of Microfabricated SiO_2 Nanotips

L Saraf,[(a)] J Young,[(a)] AS Lea,[(a)] S Thevuthasan,[(a)] G Dunham,[(b)] JW Grate,[(b)] and DR Baer[(b)]

(a) W.R. Wiley Environmental Molecular Sciences Laboratory, Richland, Washington

(b) Pacific Northwest National Laboratory, Richland Washington

The design of microfabricated SiO_2 nanotips can be crucial for applications to near-field optical microscopy as an optical fiber for high-resolution imaging applications. In this highlight, we describe a simple chemical etching technique that could be used for microfabricating these nanotips.

Microfabricated silicon/SiO_2 nanotips are useful in focused electron emission, sensors, and near-field scanning optical microscopy. Formation of nanotips can be achieved using either dry or wet chemical etching. Wet chemical etching has the specific advantage of providing reasonable control over process parameters such as etch rate and aspect ratio with uniformity over a large area and in an economical way. In the project, we used wet chemical etching to achieve anisotropic etching of silicon (100) using KOH solution and isotropic SiO_2 etching using buffered oxide etch (BOE) solution. We combined excessive (rounded) isotropic etching of SiO_2 in BOE solution with anisotropic silicon (100) etching in KOH solution to produce nanotips singly or in laterally ordered arrays.

Because of good transmission of ultraviolet light in SiO_2, these tips might be potentially useful in applications such as multiple light-transmitting apertureless nanoprobes for near-field scanning microscopy.

From a view angle of 40°, a stage prior to nanotip formation is shown in the scanning electron micrograph in Figure 1.

Thinning of the SiO_2 is apparent at the intersection of the circles, which allows eventual reduction in oxide followed by silicon wall removal underneath. The silicon (100) planes etch by undercutting the top SiO_2 layer until the silicon (100) surfaces are reached. A typical silicon/SiO_2 undercut area is shown as inset (a) of Figure 1. In a uniform periodic array of features, the length of each tip created by excessive etching roughly correlates to the radius of the excessively etched SiO_2 circles and to the separation between the features.

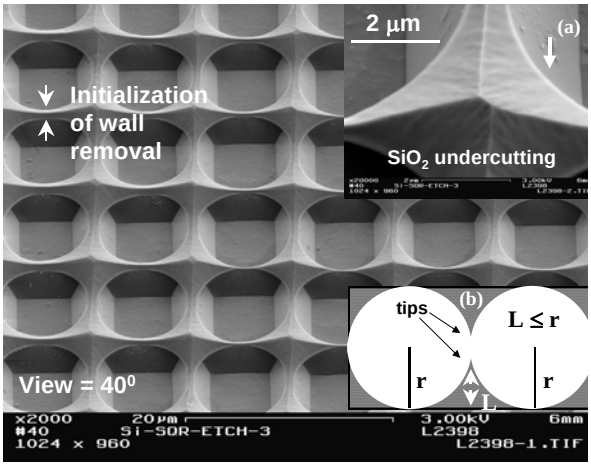

Figure 1. Scanning electron micrograph of the excessive SiO_2 etching stage, forming rounded SiO_2 patterns with rectangular bottom silicon etching. Inset (a): Close-view scanning electron micrograph (SEM) representing silicon undercutting. View angles for both micrographs are 40°. Insert (b): Schematic representing the relationship between radius of the excessively etched SiO_2 pattern and nanotip length.

A SEM image of microfabricated SiO_2 nanotips is shown in Figure 2; the viewing angle is 60°. Anisotropic etching of silicon along the (100) plane is clearly seen with a sidewall representing the silicon (111) plane. A high-resolution (100,000x) SEM of a typical nanotip from the top view is shown in Figure 1a. The sharpness of the tip is approximately 15 nm. Because a distance of 5 μm separates the original 5 μm x 5 μm square features, nanotips are observed 10 μm apart. This is shown in the optical micrograph in Figure 1b. Graded lines parallel to the edge represent a decrease in SiO_2 thickness because of the rounded nature of isotropic etching, which also causes the initial sharpness in nanotips. These nanotips were formed after 50 to 55 min etching in BOE followed by 6 hours in KOH solution.

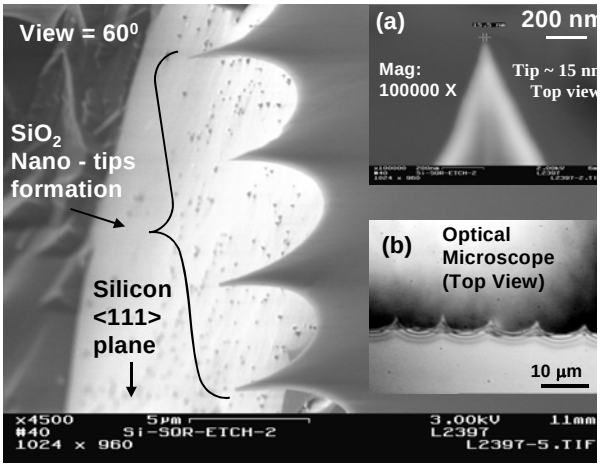

Figure 2. SEM image of laterally ordered SiO_2 nanotips with a view angle of 60°. Inset: (a) High magnification SEM of a typical SiO_2 nanotip. (b) Optical micrograph of SiO_2 nanotips from a top view representing a separation of 10 μm.

The proper SiO_2 thickness is crucial in tip formation. At lower thickness (<< 1 μm), there is a possibility that cantilevers may not survive because a firm mechanical base strength does not exist. On the other hand, higher SiO_2 thickness (>>1 μm) can result in flatness at the tip end, creating a sharp line rather than a point. Excess SiO_2 thickness also will result in longer BOE and KOH etching times during which circular SiO_2 features may merge before significant bottom silicon exposure can occur, which is required for undercutting the SiO_2. Lengths of the tips can be controlled by separation between the features. It is quite possible that by adjusting the thickness of the SiO_2 layer and the distance between features, one can sharpen these tips to a greater extent. No secondary tip-sharpening treatments are required, resulting in greater simplicity and very economical processing compared to other techniques. The flexibility in the pattern design obtained using our technique combined with controlled chemical etching steps allowed us to control even the tip orientations.

Magnetic and Transport Studies of Transition Metal Doped Semiconductor Oxides

A Punnoose,[(a)] J Hays,[(a)] V Shutthanandan,[(b)] S Thevuthasan,[(b)] R Kukkadapu,[(b)] CM Wang,[(b)] and MH Engelhard[(b)]

(a) Boise State University, Boise, Idaho

(b) W.R. Wiley Environmental Molecular Sciences Laboratory, Richland, Washington

Development of oxide dilate magnetic semiconductor materials has received considerable attention recently, and synthesis and characterization of these materials is one of the hot topics in spintronics area. This highlight describes synthesis and characterization of ferromagnetic element cobalt-doped zinc oxide material.

As part of this project, a wide variety of transition-metal-doped semiconductor oxides, such as TiO_2, SnO_2, and ZnO, have been prepared (chemically and/or using sputter deposition) and investigated.

As a remarkable result, we successfully produced ferromagnetism in powder samples of cobalt- and iron-doped SnO_2 and cobalt-doped ZnO (Figures 1 and 2) (Punnoose et al. 2003, 2004). The samples were very well characterized to ensure the phase purity and chemical composition.

The exact doping concentrations were determined using particle-induced x-ray emission experiments, carried out in collaboration with V. Shuttanandan of the W.R. Wiley Environmental Molecular Sciences Laboratory (EMSL). X-ray diffraction measurements using an in-house powder diffractometer were used to investigate changes in the lattice structure and impurity phases.

Transmission electron microscopy measurements were carried out in collaboration with C.M. Wang of EMSL to investigate changes in the particle size, shape, and morphology of the samples with transition metal-doping and preparation conditions. Selected

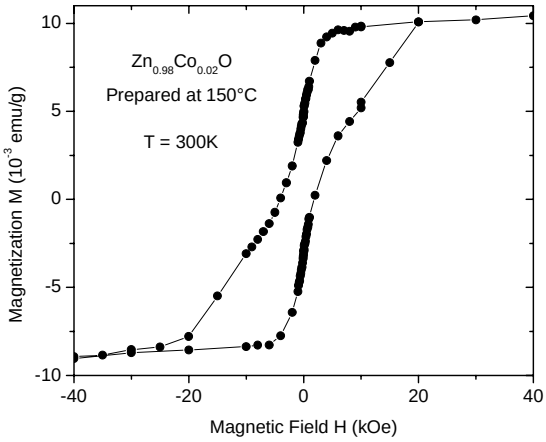

Figure 1. Room-temperature hysteresis loop obtained for a $Zn_{0.98}Co_{0.02}O$. It displays a very high coercivity (H_c ~3000 Oe) and remenance.

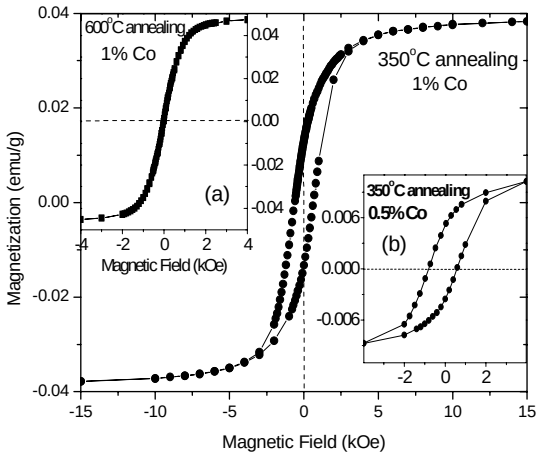

Figure 2. Room-temperature hysteresis loops obtained for $Sn_{0.99}Co_{0.01}O_2$ as a function of cobalt concentration and preparation conditions.

area electron diffraction studies were employed to further confirm phase purity. Additional structural and chemical information were obtained from x-ray photoelectron spectroscopy in collaboration with M.H. Engelhard at EMSL.

These investigations have clearly established a strong relationship between the observed magnetic and structural properties (Figure 3).

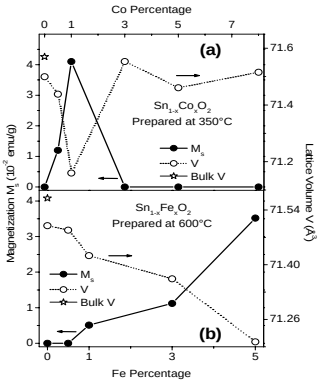

Figure 3. Saturation magnetization M_s and lattice volume V as a function of doping percentage x for (a) $Sn_{1-x}Co_xO_2$ and (b) $Sn_{1-x}Fe_xO_2$.

In $Sn_{1-x}Co_xO_2$, the lattice contracts as x increases to 0.01, and an increasing ferromagnetic behavior is observed in this regime as x increases. For x greater than 0.01, the lattice relaxes, and the ferromagnetism is completely lost in this regime. Raman spectroscopy, electron paramagnetic resonance, and x-ray photoelectron spectroscopy measurements indicate substitutional incorporation of Co^{2+} in Sn^{4+} sites for x less than or equal to 0.01. However, for x greater than 0.01, interstitial incorporation of cobalt is the predominant process (Figure 3a).

In $Sn_{1-x}Fe_xO_2$, the lattice contracts as x increases to 0.05, and an increasing ferromagnetic behavior is observed in this regime. Mössbauer spectroscopy, (in collaboration with R. Kukkadapu of EMSL) and x-ray photoelectron spectroscopy measurements indicate substitutional incorporation of Fe^{3+} in Sn^{4+} sites for x less than or equal to 0.05. (Figure 3b).

These studies enormously improved the understanding of the state and role of transition metal dopants, how their incorporation modifies the host lattice, and finally how these effects produce ferromagnetism in these systems.

References

Punnoose A, MS Seehra, WK Park, and JS Moodera. 2003. "On Room Temperature Ferromagnetism in Co-Doped TiO_2 Films." *Journal of Applied Physics* 93(10):7867-7869.

Punnoose A, J Hays, V Gopal, and V Shutthanandan. 2004. "Room-Temperature Ferromagnetism in Chemically Synthesized $Sn_{1-x}Co_xO_2$ Powders." *Applied Physics Letters* 85(9):1559-1561.

Nanoparticle-Structured Electrochemical Sensor for Detection of Metal Ions

CJ Zhong,[(a)] Y Lin,[(b)] and MH Engelhard[(c)]
(a) Binghamton University, Binghamton, New York
(b) Pacific Northwest National Laboratory, Richland, Washington
(c) W.R. Wiley Environmental Molecular Sciences Laboratory, Richland, Washington

Sensing and quantifying trace metal elements is important in health and environmental monitoring. In this study, we have explored a way of fabricating nanostructured electrochemical sensors with a three-dimensional network using functionalized gold nanoparticles. These sensors are found to have promising properties that can lead to enhanced sensitivity and selectivity for metal ion sensing.

Recent progress in the area of nanostructured materials has led to explorations of many potential technological applications such as catalysis, microelectronics, and chemical or biological recognition. One class of nanomaterials consists of core-shell-type nanoparticles with metal or oxide nanocrystal cores and organic shell encapsulation. These nanomaterials can be prepared with high monodispersity of size, enhanced stability, and chemical tunability. The use of such materials as building blocks towards molecularly wired three-dimensional ligand framework could find applications in chemical and biological sensing with enhanced interfacial sensitivity and specificity. To exploit the nanostructured materials as active components in electroanalysis, a challenging issue is how to control the ligand framework and interparticle spatial properties. We have been exploring a general strategy that entails core-shell manipulation of gold and alloy nanoparticles as building blocks towards responsive or fine-tuned interfacial materials for electroanalytical applications. Figure 1A illustrates one example system that can be prepared from gold nanoparticles and carboxylic acid functionalized alkyl thiol linkers via hydrogen-bonding linkages through an exchange-crosslinking-precipitation reaction pathway. Such a nanostructured network could lead to a spatially defined ligand framework in which void space forms channels with the nanometer-size cores defining its size and the shell structures defining its chemical specificity (e.g., L- groups provide binding sites to metal ions, M^{+n}).

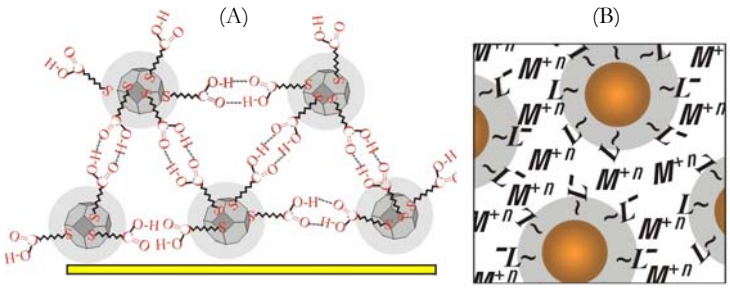

Figure 1. Schematic illustrations for (A) the carboxylic acid hydrogen-bonding linked nanoparticle assembly, and (B) the nanostructured ligand (L) framework for sensing metal ions (M).

We have shown that the nanostructured thin film could be used as an electrode coating responsive to electroactive metal ions. The cyclic voltammetric data (Figure 2) for a nanostructured film of 11-mercaptoundecanoic acid-linked gold nanoparticles of 2-nm core size (mercaptoundecanoic acid-$Au_{2\text{-nm}}$) after transferring the thin film electrode from a

previous exposure to Cu^{2+} (10-mM) solution to a 0.5-M KCl solution revealed the presence of the voltammetric waves associated with the redox reaction of copper (Figure 2b). Observation of the electroactivity provides evidence for the incorporation of Cu^{2+} into the film. The broadening of the anodic wave is also reflected by the difference in peak current between the reduction (70-μA) and the oxidation (30-μA) waves. The broad reduction wave is largely caused by the formation of copper crystals in the film. Observation of the incorporation of Cu^{2+} demonstrates that the nanostructured film could be used for pre-concentration of metal ions.

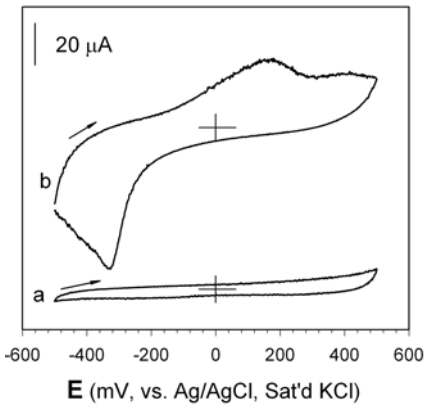

Figure 2. Cyclic voltammetric curves for MUA-$Au_{2\text{-nm}}$/GC electrode in 0.5-M KCl: a) before exposure to Cu^{2+}, and b) after exposure to 10-mM Cu^{2+}/0.5-M KCl for 10 minutes (0.28 cm^2, 50 mV/s).

The nanostructure-loaded Cu^{2+} ions can also be released by pH manipulation of the electrolyte solution. The experiments involved exposure of the thin-film electrode to an aqueous solution containing Cu^{2+} ions (1 mM), followed by treatment with a solution of pH = 2. The integrated charges from the cyclic voltammetric data (Q) for the Cu^{2+}-loaded film were 25.8 μC/cm^2 for oxidation and 120.4 C/cm^2 for the reduction wave, respectively. After the low-pH treatment, these charges were greatly reduced to 1.9 μC/cm^2 for the oxidation peaks and 5.1 μC/cm^2 for the reduction peaks, respectively. This finding is a strong indication that the incorporated Cu^{2+} ions are released in the low-pH solution. At low pH, the protonation of carboxylic acid groups weakens the binding of the Cu^{2+} ions in the film. The large difference between the quantity of charge in oxidation and reduction is indicative of the formation of copper crystals in the film.

The viability of loading metal ions into the nanostructure was further demonstrated by determination of the interfacial mass fluxes associated with the redox activity using a copper-loaded nanostructure as a model system. The MUA-$Au_{2\text{-nm}}$ thin film was coated on the piezoelectrode and pre-loaded with Cu^{2+}. The electrochemical quartz crystal nanobalance data revealed a mass change that was chemically reversible. The mass increases in the reduction sweep and decreases in the oxidation sweep. This behavior is indicative of mass loading and releasing of ionic species into and out of the film. The presence of Cu^{2+} in the copper-loaded MUA-$Au_{2\text{-nm}}$ film was further confirmed by x-ray photoelectron spectroscopy and infrared spectroscopy of the surface composition and structure. The results support the qualitative conclusion that Cu^{2+} ions are incorporated into the film via CO_2^--Cu^{2+} complexation.

In summary, we have shown that the nanostructured thin film assemblies derived from gold nanoparticles of 2-nm core size and 11-mercaptoundecanoic acid linker exhibit membrane-like properties. In these films, the hydrogen-bonding linked interparticle channels can be tuned by pH, electrode potential, and metal loading. The films are shown to be electro-chemically responsive to copper ions, which involves CO_2^--Cu^{2+} binding chemistry in the three-dimensional network. For selective sensing of a target metal ion, the three-dimensional network can be fine tuned by incorporating a specially designed ligand.

Nanoscale Effects on Ion Conductance of Layer-by-Layer Structures of Gadolinia-Doped Ceria and Zirconia

S Azad,[(a)] OA Marina,[(b)] CM Wang,[(a)] L Saraf,[(a)] V Shutthanandan,[(a)] DE McCready,[(a)] A El-Azab,[(b)] JE Jaffe,[(b)] MH Engelhard,[(a)] CHF Peden,[(b)] and S Thevuthasan[(a)]
(a) W.R. Wiley Environmental Molecular Sciences Laboratory, Richland Washington
(b) Pacific Northwest National Laboratory, Richland, Washington

Understanding the effect of interfaces in single crystal oxide multilayer films on oxygen ion-conducting properties will help us realize the effectiveness of oxide fuel cells within the intermediate temperature range. In this highlight, we demonstrate such interface effects from the perspective of conductivity.

Development of electrolyte materials that possess high oxygen ion conductance at relatively low temperatures is essential to increase the efficiency and functional life of electrochemical devices such as solid oxide fuel cells (SOFCs). The most advanced SOFCs employ oxide-ion-conducting zirconia-based electrolytes, specifically, yttria-stabilized zirconia (YSZ). The conductivity of the electrolyte determines the operating temperature of this device, which is currently around 1000ºC. Lower operating temperatures of approximately 500ºC would make SOFCs much more cost efficient and, most importantly, facilitate the practical use of SOFCs in electric vehicles. It is well established that ceria (CeO_2), doped with a divalent or trivalent cation, exhibits higher ion conductance at intermediate temperatures compared with YSZ, making ceria a promising candidate material for SOFC applications. It has been demonstrated that an increase in the interface density in a two-phase multilayered calcium and barium fluoride structure drastically enhanced the fluorine ion conductance of the material, particularly at film thicknesses in the range of 20 to 100 nm. Specifically, it was observed that this nanoscale lamellar structure exhibited higher ion conductance compared to either bulk calcium fluoride or barium fluoride along the interfacial directions at moderate temperatures when the number of heterojunctions was increased.

In this study, layer-by-layer structures of gadolinia (Gd_2O_3)-doped ceria and zirconia were synthesized on Al_2O_3(0001). The number of interfaces was varied by increasing the numbers of discrete layers, while the total film thickness was kept constant at approximately 155 nm. The films were grown in a dual-chamber ultra-high vacuum system equipped with an electron cyclotron resonance oxygen plasma source. Cesium and zirconium sources (both 99.98% purity) were evaporated from separate electron beam sources and Gd (99.98% purity) was evaporated from an effusion cell. The growth rates of the films were monitored by quartz crystal oscillators. Al_2O_3(0001) single crystal substrates were ultrasonically cleaned in acetone and methanol prior to insertion into the dual-chamber ultra-high vacuum system through a load lock. Inside the molecular beam epitaxy chamber, the substrate surfaces were cleaned at 875 K for 10 minutes in activated oxygen from the electron cyclotron resonance plasma source at an oxygen partial pressure of about 1.5×10^{-5} Torr. The gadolinia-doped epitaxial structures of CeO_2 and zirconia layers were grown on Al_2O_3 substrates by alternate evaporation of cesium and zirconium metals in the presence of a low-pressure oxygen plasma.

Several *in situ* and *ex situ* characterization techniques were used to characterize these films. The results indicated that these layered films were predominantly oriented along the (111)

direction. The total thickness of each film was confirmed as approximately 155 nm. The gadolinium concentration in the CeO_2 and zirconia layers was found to be 12 atomic percent. High-resolution transmission electron microscopy measurements showed that the layered structures contained structural domains within each layer as well as internal and interfacial dislocations between the layers.

Total conductivity, which is of the sum of the electronic and oxygen ionic conductivity in these layered films, was measured as a function of temperature using a four-probe van der Pauw technique. Because the electronic conductivity in these oxides is significantly less compared to ionic conductivity, especially at low temperatures, ionic conductivity dominates in these materials. As such, the total conductivity will be identified as oxygen ionic conductivity in this paper. Oxygen ionic conductivity results for 2-, 4-, 8-, 10- and 16-layered Gd_2O_3-doped CeO_2 and ZrO_2 films on Al_2O_3(0001) substrates are shown in Figure 1 (left plot). The oxygen ionic conductivity data from polycrystalline YSZ and single crystal YSZ are also shown for comparison (Figure 1, right plot). In general, these highly oriented films showed much higher conductivity compared to bulk polycrystalline YSZ. It is apparent from the impedance spectra that increasing the number of interfaces (i.e., the number of discrete layers) in the structure facilitates ion transport and leads to an increase in the oxygen ionic conductivity at low temperatures. The ionic conductivities for single crystal YSZ and the 2-, 4-, 8-, 10- and 16-layered films, all at 650 K extracted from the Figure 1 (left plot) are shown in Figure 1 (right plot). At that temperature, increasing the number of layers resulted in higher oxygen ionic conductivity up to a thickness of 15 nm (for individual layers), beyond which conductivity decreases. The maximum value for the conductivity appears to be at least an order of magnitude higher than that from either polycrystalline gadolinium-doped bulk CeO_2 or a single crystal YSZ thin film.

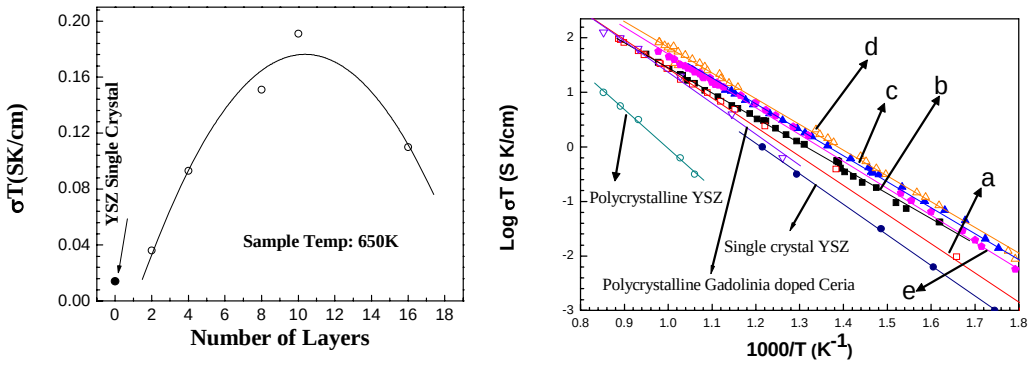

Figure 1. Left plot: Arrhenius plots of oxygen ionic conductivity of 2- a), 4- b), 8- c), 10- d) and 16-layer e) gadolinium-doped ceria-zirconia thin films. The data from polycrystalline and single-crystal YSZ are also displayed in this plot. Right plot: Conductivities of single crystal YSZ, 2-, 4-, 8-, 10- and 16-layer films at 650 K.

Photochemical Charge Transfer and Trapping at the Interface Between an Organic Adlayer and an Oxide Semiconductor

MA Henderson,[(a)] JM White,[(a)] H Uetsuka,[(b)] and Y Onishi[(a)]
(a) Pacific Northwest National Laboratory, Richland, Washington
(b) Kanagawa Academy of Science and Technology, Kawasaki, Japan

The use of oxides for photocatalytic water splitting, pollutant destruction, and bacterial disinfection has recently received considerable attention. This highlight describes the identification of surface sites associated with charge transfer and trapping during photo-decomposition of an organic layer on a TiO_2(110) surface.

Photocatalysis on oxides has attracted considerable attention because of its possible application for water splitting, pollutant destruction, and bacterial disinfection. These processes are catalyzed using photon-excited, electron-hole pairs that perform surface-mediated redox chemistry. Little is known at the site-specific level about interfacial charge transfer and trapping because most heterogeneous photocatalyst surfaces possess a complex and poorly defined distribution of sites and the media in which typical studies are performed (aqueous or high-pressure conditions) are inhospitable to many molecular-level probes. We have identified surface sites associated with charge transfer and trapping during photo-decomposition of an organic adsorbate. Trimethyl acetic acid (TMAA) was used as a model organic material, and Figure 1 shows scanning tunneling microscope images obtained at 280 K for various stages of ultraviolet irradiation of a trimethylacetate (TMA)-covered TiO_2(110) surface.

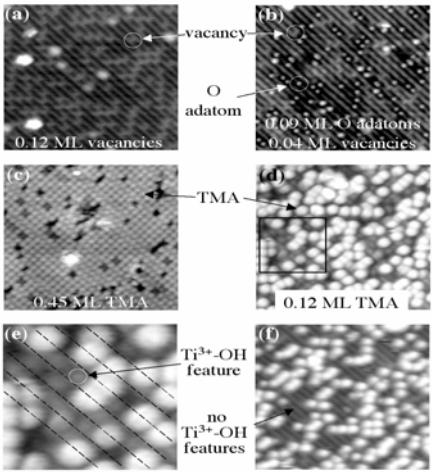

Figure 1. Scanning tunneling microscope images of trimethylacetate -covered TiO_2(110) at 280 K: a) Clean TiO_2(110) annealed in ultrahigh vacuum; b) 'a' exposed to 100 L O_2; c) saturation of 'b' with TMA; d) irradiation of 'c' in ultrahigh vacuum for 1 hour with a 300-W Xe arc lamp; e) square region indicate in 'd'; and f) 'd' exposed to 100 L O_2. Image sizes (with exception of 'e') are 16 x 16 nm.

Image (a) in Figure 1, obtained from the vacuum annealed surface, shows an oxygen vacancy (example circled) population of 0.12 ML (1 ML = 5.2 x 10^{14} sites/cm^2). The large bright spots are unidentified impurities. The bright and dark rows correspond to surface Ti^{4+} and bridging O_2- sites, respectively. Image (b) shows that a 100-L O_2 exposure at 280 K oxidized about two-thirds of the vacancy sites and deposited an equivalent number of oxygen adatoms (example circled) at Ti^{4+} sites. TMAA exposure resulted in a dense TMA adlayer (image [c]), where the O adatoms blocked some TMA adsorption sites (empty spaces). Ultraviolet irradiation for 1 hour (image [d]) decomposed 0.33 ML of TMA and resulted in a change in the TMA spot size possibly associated with the change in TMA coverage or with a tip-related change. Also, faint spots appeared among the remaining TMA spots. Expansion of the square

region in image (d) shows that the faint spots (example circled) were present at about 50% of the level of the depleted TMA, and with Ti^{3+}-OH, groups disappeared revealing the underlying clean TiO_2(110) surface (image [f]).

Figure 2, taken from an oxidized surface saturated at room temperature with TMAA, shows that the electronic region is devoid of signal between the phonon tail (less than 0.5 eV) and the onset of band-to-band excitation of TiO_2 (greater than 3.2 eV, not shown).

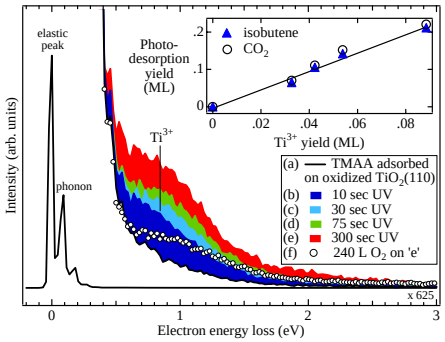

Figure 2. Electron energy-loss spectroscopy spectra from TMA-covered TiO_2(110), oxidized prior to TMAA adsorption: (a) TMA-covered surface prior to exposoure to ultraviolet irradiation; (b-e) after irradiation with a 100-W Hg arc lamp; (f) Exposure of 'e' to 240 L O_2. Inset: Correlation between the isobutene and CO_2 photodesorption yields and the Ti^{3+} signal generated during photolysis.

Ultraviolet irradiation of the TMA-covered surface in the absence of oxygen resulted in a feature at about 0.8 eV (spectrum [b]) that grew with additional ultraviolet irradiation (spectra [c-e]). This feature is indicative of Ti^{3+}, in this case resulting from photogenerated electrons trapped at the surface of TiO_2(110) as Ti^{3+}-OH groups. Irradiation of the clean, oxidized TiO_2(110) surface with ultraviolet radiation did not result in any new features ascribable to Ti^{3+}. As in the case of the scanning tunneling microscope data in Figure 1(f), the Ti^{3+} signal arising from photodecomposition of TMA was largely removed by post-exposure to oxygen (spectrum [f]). Using the Ti^{3+} electron energy-loss spectroscopy signal intensity from the vacuum annealed surface as a standard, we correlated the amount of Ti^{3+} generated during ultraviolet photodecomposition of TMA with the isobutene (from t-butyl radical conversion) and CO_2 photodesorption yields. The latter were calibrated using the thermal desorption signals from saturated monolayers on the TiO_2(110) surface at 100 K. The inset in Figure 2 shows that the accumulation of Ti^{3+} increased linearly with the amount of photodesorption product. The ratio between photodesorbed isobutene/CO_2 and Ti^{3+} was about 2:1.

The scheme in Figure 3 illustrates the two redox channels associated with ultraviolet photodecomposition of TMA on TiO_2(110). TMAA adsorbs via decomposition of the O-H bond, generating a bridging TMA and a bridging OH group. Whole transfer to TMA results in decarboxylation. Electrons trap at surface cations based on scanning tunneling microscope and electron energy-loss spectroscopy results.

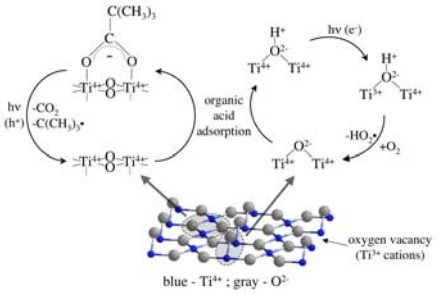

Figure 3. Reaction scheme illustrating the separate redox processes associated with photodecomposition of TMAA on TiO_2(110), along with the sites associated with charge transfer and charge trapping.

The role of oxygen in this process involves titrating the accumulated trapped electrons to reoxidize the surface, presumably via H• abstraction from the bridging OH sites bound at Ti^{3+} sites. The product is likely a short-lived HO_2• species that reacts at room temperature to form gaseous water and adsorbed O adatoms. These data reveal that charge transfer and trapping channels can be tracked on a model TiO_2 photocatalyst using molecular-level probes.

Probing Quantum Anti-dots and Au Nanoclusters in $SrTiO_3$

CM Wang,[(a)] V Shutthanandan,[(a)] Y Zhang,[(a)] S Thevuthasan,[(a)] and G Duscher[(b)]
(a) W.R. Wiley Environmental Molecular Sciences Laboratory, Richland, Washington
(b) North Carolina State University, Raleigh, North Carolina

Metal particles dispersed in a dielectric will change the optical properties of the material. The change may be caused by the formation of quantum anti-dots at the vicinity of the metal particles. Adding to the knowledge base of fundamental material science, this paper presents atomic-level observations of the formation of quantum anti-dots.

Ion implantation and subsequent high-temperature annealing is an effective way to prepare metal nanoclusters dispersed in a dielectric for useful optical and electrical properties. However, there is very little understanding of the nucleation and growth process of these nanoclusters, their correlations with the sites of the implanted ions, and the behavior of defects (such as vacancies) generated during the ion-implantation process. Using high-angle annular dark-field imaging in aberration-corrected scanning transmission electron microscopy, we directly observed that at a dilute concentration, gold atoms implanted in $SrTiO_3$ are in a substitutional lattice position for both strontium and titanium (Figure 1). Congregation of gold atoms by diffusion to a critical concentration leads to the nucleation of a gold lattice within the $SrTiO_3$. The gold nanocluster and $SrTiO_3$ were found to maintain an orientation relationship of gold [001]//$SrTiO_3$[001] and gold (100)//$SrTiO_3$(100), which corroborated the results of a first-principles, total-energy calculation. The interface between the Au cluster and $SrTiO_3$ was bridged by an O/Ti plane. The Au-O bond length was found to be 2.2 Å, which is the same as the Au-O bond length in AuO. Furthermore, the atomic planes adjacent to the interface in both gold and $SrTiO_3$ were found to be slightly stretched. The high concentration of vacancies generated during the gold implantation aggregated to form cavities in the $SrTiO_3$ lattice, and were faceted mostly along the $SrTiO_3$ {100} and (110) planes. The gold and vacancy clusters were spatially associated, indicating a strong interaction. Thus, the formation of cavities in gold-implanted materials indicates that the vacancy-clustering process prevails over the Frenkel-pair recombination.

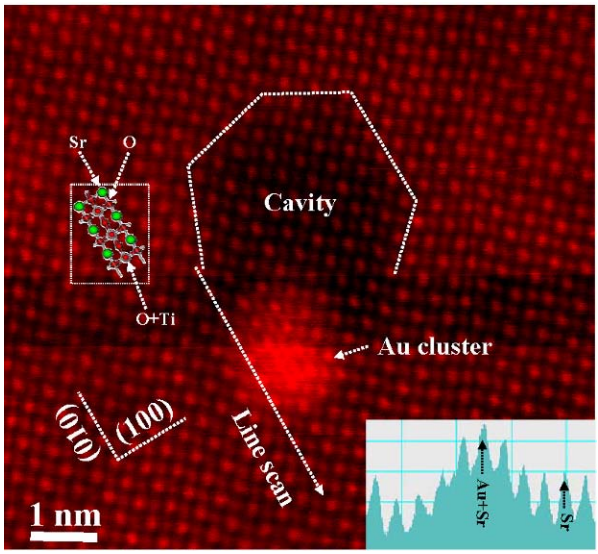

Figure 1. Gold atom distribution in strontium titanate (STO) observed by high resolution scanning transmission electron microscopy.

Proton Transfer Reaction Mass Spectrometry Characterization of Diesel Engine Exhaust

ML Alexander,[(a)] BT Jobson,[(a)] GG Muntean,[(a)] CL Aardahl,[(a)] GD Maupin,[(a)] TA Gallant,[(a)] J Storey,[(b)] and B Patridge[(b)]

(a) Pacific Northwest National Laboratory, Richland, Washington

(b) Oak Ridge National Laboratory, Oak Ridge, Tennessee

Real-time analysis of diesel exhaust is an important new development in the evaluation of new technologies, such as catalysts, designed to make diesel engines cleaner and more efficient.

An important new application of the proton transfer reaction mass spectrometer (PTR-MS) at the W.R. Wiley Environmental Molecular Sciences Laboratory has been the real-time on-line characterization of organic compounds present in diesel exhaust. Most existing online instrumentation for analysis of diesel emissions has focused on inorganic species due to the lack of a real-time instrument, such as PTR-MS, capable of making quantitative on-line measurements of organic compounds. The key goal of this research has been to understand the complex organic mass spectra produced by diesel exhaust at a sufficient level of detail so the PTR-MS can be used as a tool for answering critical questions presented by current engine catalysis research and development efforts.

Two types of diesel engines were sampled by the PTR-MS using mass scans made from 21 to 210 m/z at different engine loadings. Initial measurements were made by dilution of exhaust from a diesel generator prior to sampling by the PTR-MS. The PTR mass spectrum for the generator engine under idle conditions is shown in Figure 1.

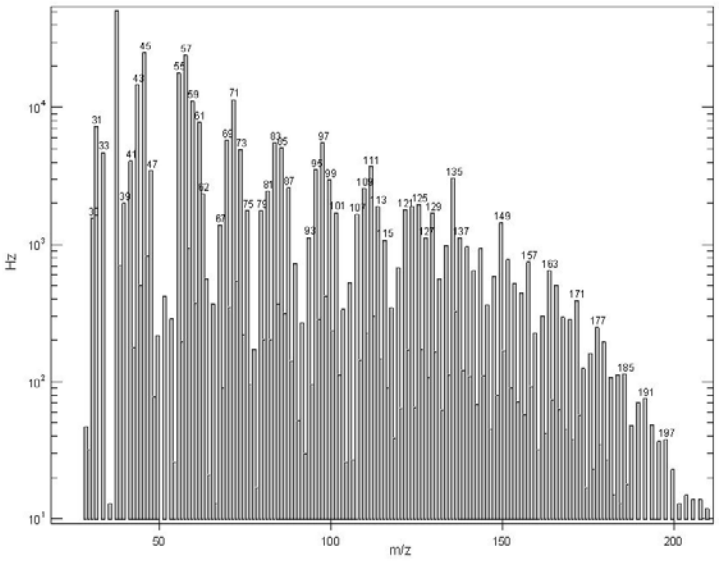

Figure 1. PTR-MS scan of diesel engine generator exhaust operating at no load. Ion signal intensity in counts per second (Hz) are plotted against mass to charge ratio (m/z).

Background count rates have been subtracted, removing major ions produced in the ion source such as m/z 21, 32, 37, and 55. The mass spectrum is complex, with a peak at every mass, with even numbered masses dominating. Count rates for most masses increased as engine load decreased. This is in contrast to the soot concentration, which increased with engine load. Understanding the fragmentation of alkanes in the PTR-MS data is a key factor in interpreting the mass spectrum. The mass spectrum was complex

and showed a strong pattern of 14n+1 peaks with a relative abundance similar to that obtained from electron impact ionization of alkanes. Further experiments verified that the H_3O^+ proton transfer reaction with n-alkanes under the conditions of the drift resulted in fragmentation patterns nearly identical to those of electron impact. Alkane fragmentation likely simplified the upper end of the mass spectrum, and reduced the mass interference with isobaric aromatics. Tentative identification of several aromatic species and light alcohols and aldehydes was made. It is shown that the concentrations and relative abundances of hydrocarbons changed as a function of engine load. Concentrations of aldehydes and ketones dominated the exhaust emissions. The relative abundance of alkanes, aromatics, aldehydes, and alcohols as determined by PTR-MS was broadly consistent with published data from gas chromatography analysis. About 75% of the PTR-MS organic ion signal could be assigned.

Further measurements were made inside the catalyst of a Volkswagen Passat® at several locations using spatially resolved MS techniques (SPACI-PTR-MS). The results from this study are still being evaluated; however, Figure 2 shows a sample of the preliminary results.

While the data from m31 and m57 show the expected behavior—little catalyst effect at low temperature with full oxidation at high temperature—the behavior of benzene was erratic and often the reverse of what was expected. The other clear result is that at high operating temperature when the catalyst is most efficient, only the first centimeter or less of the catalyst is needed for complete oxidation of organics. *In situ* measurements of diesel exhaust in diesel catalysts using the SPACI-PTR-MS techniques will be continued during 2005.

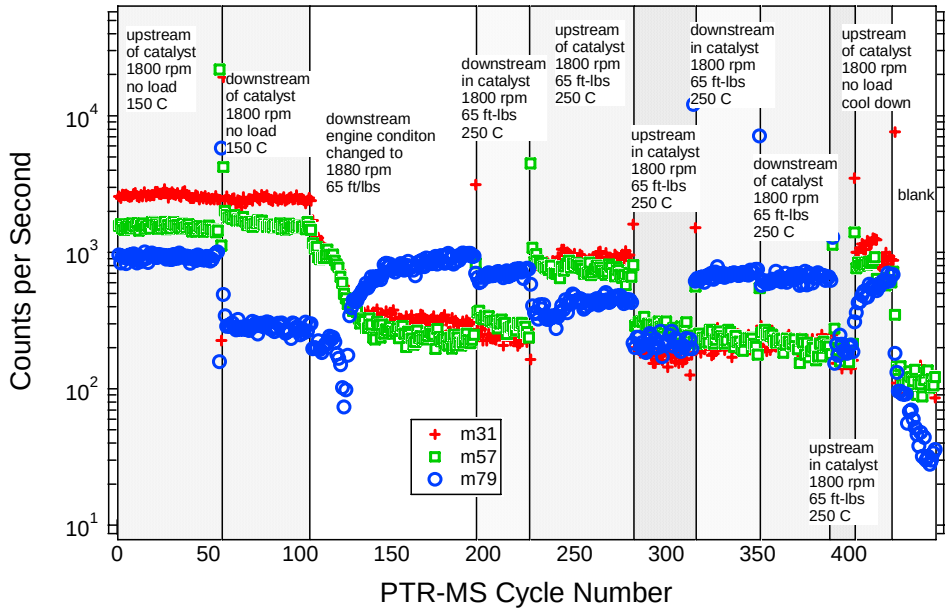

Figure 2. Preliminary data from SPACI-PTR-MS measurements in diesel catalyst for formaldehyde (m31), an alkane fragment (C4H9+ m57), and benzene (m79).

Synthesis and Characterization of Dendrimer-Derived Monometallic Ruthenium and Bimetallic Platinum-Ruthenium Catalysts

G Lafaye,[(a)] S Chin,[(a)] MH Engelhard,[(b)] CT Williams,[(a)] and MD Amiridis[(a)]
(a) University of South Carolina, Columbia, South Carolina
(b) W.R. Wiley Environmental Molecular Sciences Laboratory, Richland, Washington

This research focuses on the area of heterogeneous catalysts for the production and purification of hydrogen for fuel cell applications.

The supported catalyst plays a central role in industrial chemical processes, as well as in pollution abatement. In such catalysts, the average particle size and particle-size distribution of the supported nanoparticles is often critical for controlling the catalytic performance (i.e., activity and/or selectivity). Recently, dendrimers were successfully used to template and stabilize metal nanoparticles in solution (Figure 1). Dendrimers are hyperbranched polymers with a specific molecular structure, which are particularly well-suited for hosting metals for the following reasons: 1) the dendrimer templates themselves are of fairly uniform composition and structure, and therefore, they can yield well-defined nanoparticles reproducibly; 2) the nanoparticles are stabilized by encapsulation within the dendrimer, and therefore, they do not agglomerate; 3) the terminal groups of the dendrimer periphery can be tailored to control solubility of the hybrid nanocomposites, and therefore, they can be used as handles for facilitating linking to surfaces and other polymers.

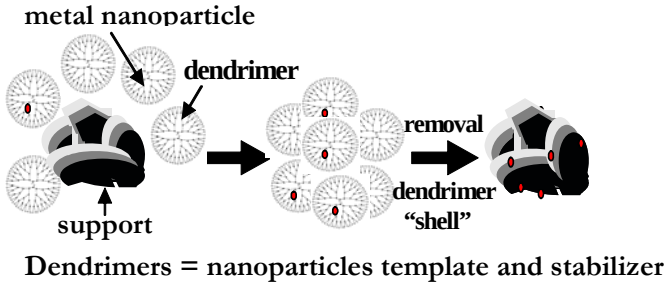

Figure 1. Metal nanoparticles supported by dendrimers.

Hydroxyl-terminated polyamidoamine (PAMAM) dendrimers include interior tertiary amine groups that can chelate metal ions. Following complexation of the metal ions with the dendrimer amine groups, a reduction step can yield to dendrimer-encapsulated metal nanoparticles. Deposition of the metal-dendrimer nanocomposites onto an oxide support and removal of the dendrimer 'shell' by thermal treatment can lead to supported catalysts with a very narrow particle-size distribution.

Results of previous studies have indicated that Pt^{4+} ions (from a H_2PtCl_6 precursor) can complex with a PAMAM dendrimer. Ultraviolet-visible spectroscopic results indicate that Ru^{3+} ions (from a $RuCl_3$ precursor) are also capable of complexing with the dendrimer structure. In a subsequent reduction step, the Ru^{3+} ions yield finely dispersed ruthenium

nanoparticles with a narrow particle-size distribution. These dendrimer-stabilized nanoparticles were then deposited onto an Al_2O_3 support and thermally activated to remove the dendrimer 'shell.'

Despite some mild sintering observed during this activation process (Figures 2a and 2b), high-resolution transmission electron microscopy (HRTEM) measurements indicate that the resulting ruthenium Al_2O_3 catalyst has a smaller average metal particle size and a narrower particle-size distribution than a similar catalyst prepared by a traditional wet impregnation from the same $RuCl_3$ precursor (Figures 2b and 2c).

In the course of the preparation of supported bimetallic catalysts, the main difficulty is to create an intimate contact between the two metals to obtain a synergistic catalytic effect. Classical co-impregnation or successive impregnations often prove to be unsatisfactory because metal segregation is frequently observed. We have investigated the synthesis of bimetallic platinum/ruthenium catalysts via the dendrimer method following either co-complexation/co-reduction or sequential complexation/reduction protocols. Energy dispersive x-ray microanalysis of supported platinum/ruthenium/Al_2O_3 catalysts thus obtained reveals that truly bimetallic particles are formed in both cases. Sequential complexation can result in selective surface enrichment of one of the two metals with direct consequences on the catalytic properties of the resulting materials. In fact, despite their similar particle-size distributions (obtained via HRTEM measurements), x-ray photoelectron spectroscopy and Fourier transform infrared spectroscopy studies of adsorption carbon monoxide reveal that the structure and surface properties of these platinum/ruthenium catalysts are strongly affected by the preparation protocol.

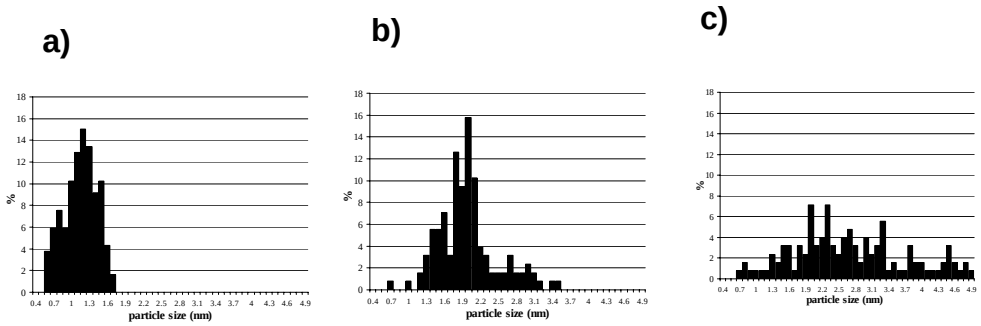

Figure 2. Metal particle-size distributions of a) Ru-G4OH PAMAM nanocomposites in solution, b) a 1wt% ruthenium/Al_2O_3 catalyst prepared from a ruthenium dendrimer precursor and reduced for 2 hours at 300°C, and c) a 1wt% ruthenium/Al_2O_3 catalyst prepared directly from a $RuCl_2$ precursor and reduced for 2 hours at 300°C.

Synthesis of Room-Temperature Ferromagnetic Chromium-Doped TiO_2(110) Rutile Single Crystals Using Ion Implantation

V Shutthanandan,[(a)] S Thevuthasan,[(a)] T Droubay,[(b)] SM Heald,[(b)] MH Engelhard,[(a)] DE McCready,[(a)] SA Chambers,[(b)] P Nachimuthu,[(c)] and BS Mun[(c)]

(a) W.R. Wiley Environmental Molecular Sciences Laboratory, Richland, Washington
(b) Pacific Northwest National Laboratory, Richland, Washington
(c) Lawrence Berkeley National Laboratory, Berkeley, California

Development of oxide dilute magnetic semiconductor materials has recently received considerable attention, and systems and characterization of the materials are among the primary interests in the field of spintronics. This highlight describes systems of chromium-doped titanium dioxide using ion implantation and characterization of the material using various bulk and surface-sensitive capabilities.

There is growing interest in synthesizing new diluted magnetic semiconductor materials because of their potential to efficiently inject spin-polarized carriers into nonmagnetic semiconductor heterostructures in spin-based devices. It has recently been shown that certain oxide semiconductors doped with magnetic transition elements show room-temperature ferromagnetism. In particular, cobalt-doped TiO_2 appears to be the most promising candidate in terms of exhibiting a high curie temperature. Several synthesis methods have been used to grow these materials in both anatase and rutile phases. However, care must be taken to avoid growth methods and conditions that promote the formation of cobalt nanoparticles. We have recently shown that ferromagnetic chromium-doped TiO_2 anatase and rutile films can be synthesized using oxygen-plasma-assisted molecular beam epitaxy (OPA-MBE).

Single-crystal rutile TiO_2(110) substrates purchased from Princeton Scientific Corporation were implanted with 100-keV Cr^+ ions at Implant Sciences Corporation at a substrate temperature of 975 K and an ion fluence of 1.25×10^{16} ions/cm^2. Following implantation, the samples were characterized by vibrating sample magnetometry to determine the magnetic properties, and a four-point probe to determine resistivity. Also, the structural and compositional properties were determined by Rutherford backscattering spectrometry, proton-induced x-ray emission, x-ray photoelectron spectroscopy depth profiling, and x-ray diffraction. Chromium and titanium L-edge and oxygen K-edge x-ray absorption near-edge spectroscopy (XANES) in both total electron yield and total fluorescence yield was measured at the Berkeley Advanced Light Source. In addition, chromium K-edge XANES measurements were made at the Argonne Advanced Photon Source using the PNC-CAT beamline.

A typical vibrating sample magnetometry hysteresis loop taken at room temperature from a chromium-implanted TiO_2(110) rutile sample is shown in Figure 1. The magnetic field was oriented perpendicular to the sample surface. However, there were no noticeable differences between in-plane and perpendicular magnetization loops. The sample shows clear

ferromagnetic behavior with a saturation magnetization of approximately 0.29 μB/ chromium atom, assuming that all the chromium atoms contribute to the magnetization. This value is less than that found for chromium-doped TiO_2 anatase grown by molecular beam epitaxy (approximately 0.6 μB/chromium atom). The coercive field was found to be approximately 150 Oe and the remanent magnetization on the order of approximately 20%. This sample was also semiconducting because of reduction associated with high-temperature implantation, with a resistivity of 360 μΩ-cm.

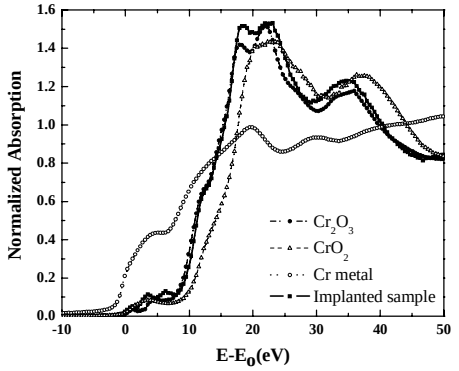

Figure 1. Room-temperature vibrating sample magnetometry hysteresis loop for approximately 1 at% chromium-implanted TiO_2 (110) rutile.

Chromium metal is antiferromagnetic; however, CrO_2 is a half metal. Therefore, the presence of CrO_2 must be carefully monitored to ensure that the observed ferromagnetic response is not caused by this phase. To this end, we employed chromium L-edge and K-edge XANES to determine the valance state of implanted chromium. Chromium K-edge XANES spectra from chromium-implanted rutile TiO_2 and various chromium-containing reference materials (chromium metal, Cr_2O_3, and CrO_2) are shown in Figure 2. It is clear that the spectrum for chromium-implanted TiO_2 strongly resembles that of Cr_2O_3. Both spectra show the small pre-edge feature resulting from a dipole-forbidden 1*s*-3*d* transition and an absorption edge at $E\text{-}E_o$= 12 V. In addition, spectra obtained from chromium metal and CrO_2 are qualitatively different from that of chromium-implanted TiO_2. There is thus no detectable chromium (0) and/nor Co(IV) in the implanted sample. Hence, the majority of the chromium atoms are in the $^{+}3$ formal oxidation states. Substitution of chromium (III) for titanium (IV) requires one neutral O vacancy (or doubly occupied F center) for every two chromium (III) ions to maintain charge neutrality.

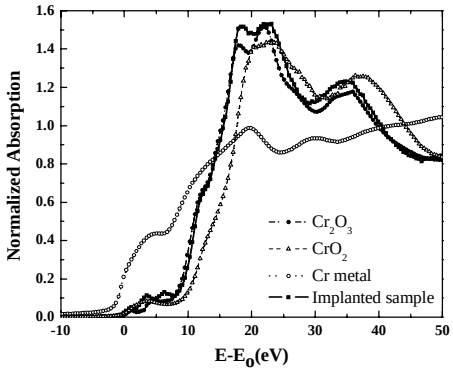

Figure 2. Chromium K-edge XANES spectra from chromium metal, CrO_2, Cr_2O_3 and chromium-implanted rutile TiO_2.

Distinguishability of Oxygen Desorption from the Surface Region with Mobility-Dominant Effects in Nanocrystalline Ceria Films

L Saraf,[(a)] V Shutthanandan,[(a)] Y Zhang,[(a)] S Thevuthasan,[(a)] CM Wang,[(a)] A El-Azab,[(b)] and DR Baer[(b)]

(a) W.R. Wiley Environmental Molecular Sciences Laboratory, Richland, Washington
(b) Pacific Northwest National Laboratory, Richland, Washington

Oxygen desorption from the ceria grain surface is of fundamental interest to researchers working in the area of catalysis and oxide fuel cells. Studying such oxygen desorption with the help of nuclear reaction analysis gives us an additional tool to use for studying desorption properties as a function of film depth. In this study, we clearly distinguished oxygen desorption from the surface region of nanocrystalline ceria films grown by a sol-gel technique.

Understanding and controlling reversible oxygen storage properties of nanocrystalline ceria is important because of its potential applications in solid oxide fuel cells and catalysis. In the case of thin films, most of the techniques commonly used to study its reducibility do not provide depth-dependent information. Ion beam-based methods such as nuclear reaction analysis (NRA) can be effectively used to quantify the oxygen content as a function of film depth and temperature. Here, we have used NRA to distinguish oxygen desorption from the surface region of approximately 3 nm average grain size, 1-μm-thick ceria films. In an NRA experiment, oxygen uptake was carried out at 200ºC, 300ºC, 400ºC, and 600ºC at a background ^{18}O pressure of 4.0 x 10^{-6} Torr. Uptake times were 10, 40, and 70 minutes at each temperature. Total uptake was determined using $^{18}O(p,\alpha)^{15}N$ nuclear reaction at room temperature.

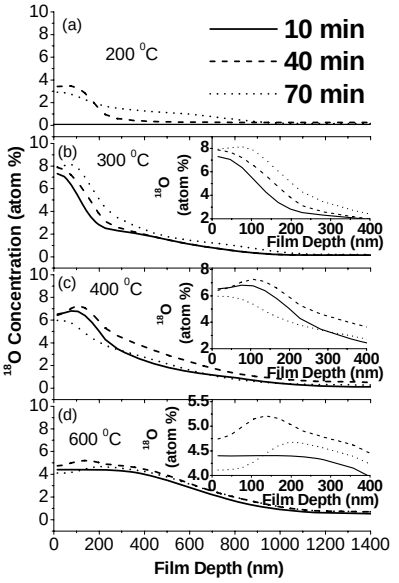

Figure 1. Individual ^{18}O uptake measurements as a function of CeO_2 film depth at (a) 200ºC, (b) 300ºC, (c) 400ºC, and (d) 600ºC. Solid, dashed, and dotted lines represent measurements taken after 10 min, 40 min, and 70 min uptake times, respectively. Insets b-d are enlarged areas of the spectra near the surface region.

Individual ^{18}O depth profiles for exposure at the temperatures identified above are shown in Figure 1 (a-d, respectively). To clearly show changes in ^{18}O distribution near the surface, insets represent enlarged areas of the spectra near the surface region. No major shift in the oxygen concentration maxima is observed at 300ºC; however, oxygen maxima were observed to be shifted at 400ºC and 600ºC. The depth profile slopes and oxygen concentration analysis of the curves in region I (0 to 450 nm) and region II (500 to 900 nm) are represented in Figure 2(a, b).

Slope values ($\Delta^{18}O/\Delta d$, d = film depth) of the each individual depth profiles in regions I and II as a function of oxygen uptake temperature are given in Figure 2(a). Maximum oxygen concentrations in regions I and II as a function of uptake temperatures are represented in Figure 2(b). Slope values and oxygen concentrations are observed to reach maxima at 300ºC in region I. On the contrary, an overall linear increase in the slope and the oxygen concentration is observed in region II.

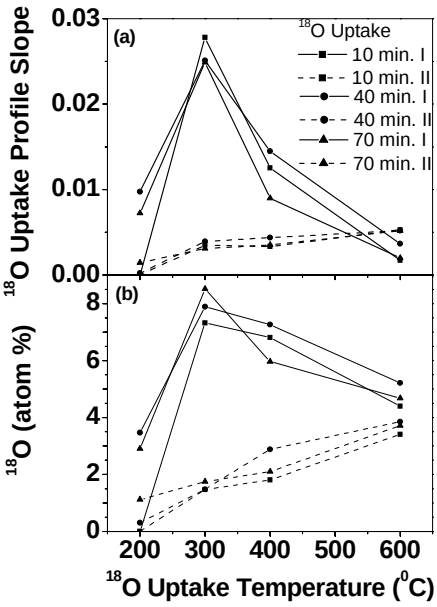

Figure 2. (a) Maximum value of slopes in regions I and II as a function of oxygen uptake temperatures. (b) Maximum values of oxygen concentration in regions I and II as a function of oxygen uptake temperatures. Regions I and II were considered from 0 to 450 nm and 500 to 900 nm, respectively. The slopes were calculated by fitting straight lines through the oxygen depth profile data points.

In general, rapid diffusion and permeation of ^{18}O through the film can be enhanced because of porosity and the presence of amorphous regions around nano-crystals. Oxygen uptake time and temperature are two major factors that affect the overall complex transport process. Temperature effects are expected to dominate over the time effects because of rapid variation in diffusion rate with temperature. Because the oxygen uptake and anneal measurements were carried out at the background ^{18}O pressure of 4.0×10^{-6} Torr and oxygen-free 1.0×10^{-8} Torr, respectively, the proximity of low pressure near the film surface region is the potential cause for the oxygen loss. A shift in the oxygen concentration maxima toward the interface (Figure 1) with an increase in uptake temperature corresponds to oxygen desorption from the film surface region into the vacuum.

The similarity of ^{18}O distribution slopes and oxygen intensities in regions I and II (as shown in Figure 2 a, b) demonstrates a unique behavior of oxygen transport in ceria films. At 200ºC, lower intensity of oxygen concentration as well as lower slope values represent higher surface adsorption barrier. At 300ºC, adsorption of oxygen into CeO_2 is enhanced, but desorption and diffusion rates are slower, thus limiting oxygen mobility and resulting in large ^{18}O concentration in region I. Improved oxygen mobility in the temperature range of 400 to 600ºC can allow accumulated oxygen in the surface region to redistribute in the ceria film, causing intensity increase in region II. The loss of oxygen from a particular nanograin in the film interior also can be easily accepted in the surrounding nanograins, making it difficult to distinguish any individual contribution to the oxygen redistribution. Additionally, defect density, dominant crystallographic orientation, and grain-boundary density also are expected to play important roles in this process.

User Projects

Field-Emission Scanning Electron Microscope Investigation of Anode-Supported, Yttrium-Stabilized Zirconia Fuel Cells Poisoned by Chromium

SP Simner
Pacific Northwest National Laboratory, Richland, Washington

Surface and Interface Study of Contacts to Carbon-Based Films

LM Porter, PB Kulkarni
Carnegie Mellon University, Pittsburgh, Pennsylvania

Determination of the Catalytic Properties of Metal Coated Nanowires

AD LaLonde, MG Norton
Washington State University, Pullman, Washington

Modification of Structure and Selectivity of Sensing Layers

M Josowicz
Georgia Institute of Technology, Georgia Tech Research Corporation, Atlanta, Georgia

Surface Characterization of Ambient Ultrafine Particles

EL Bullock, AM Johansen, C Thomas-Bradley
Central Washington University, Ellensburg, Washington

Stability of H Species in Various Dielectric Films Used in Advanced Microelectronic Fabrication

YR Kuan
Texas Instruments Incorporated, Dallas, Texas

Surface Area and Porosity Analyses of Mesoporous Thin Films and Powders

RD Champion, S Li, AR Courtney
Pacific Northwest National Laboratory, Richland, Washington

Scanning Electron Microscope Investigation of Thermal Barrier Coatings and Oxide-Dispersion-Strengthened Alloys

GJ Grant
Pacific Northwest National Laboratory, Richland, Washington

Transmission Electron Microscope Study on Solid Oxide Fuel Cell Interconnects

Z Yang
Pacific Northwest National Laboratory, Richland, Washington

Deposition of Actuve Boron Carbide Thin Film by Plasma Enhances Chemical Vapor Deposition

SN Kundu
Pacific Northwest National Laboratory, Richland, Washington

An Experimental and Data Analysis Investigation into the Trapped Gases and Non-Ice Material in the Surfaces of the Outer Planets Icy Satellites

CA Hibbitts
Planetary Science Institute, Pasadena, California

Investigation of Oxygen Diffusion in Single Crystal $SrTiO_3$ Films Grown on Silicon

ZJ Yu
Motorola, Tempe, Maryland

Characterization of Mesoporous Silicon Dioxide Particles for the Characterization of Non-Ideal Sorption Behavior

DR Yonge, DL Washington
Washington State University, Pullman, Washington

Electrochemical Sensors and Biosensors for Environmental and Health Monitoring

J Xu
Nanjing University, Nanjing, China

Electrochemical Detection of Lead in Saliva

W Yantasee
Pacific Northwest National Laboratory, Richland, Washington

Trace Metal Composition of Cobalt

JB Cliff
Pacific Northwest National Laboratory, Richland, Washington

A Combinatorial Sputtering Approach to Magnetic Properties Modification of FeCoB

RR Owings, DP Pappas
National Institute of Standards and Technology, Boulder, Colorado

Study of Martensitic Transformations in Shape Memory Alloys by Real-Time Measurement of Surface Work Function Change

M Cai, JT Dickinson
Washington State University, Pullman, Washington

X-Ray Photoelectron Diffraction of Magnesium Oxide (111)-(1x1)

RA Plass
Sandia National Laboratory, Albuquerque, New Mexico
M Gajdardziska-Josifovska
University of Wisconsin, Milwaukee, Milwaukee, Wisconsin

Chemical Characterization of Sub-Micrometer Mineral Phases in Extraterrestrial Materials Previously Characterized by Nano-Secondary Ion Mass Spectroscopic Isotope Imaging
FJ Stadermann
Washington University, St. Louis, Missouri

Advanced Electrode Concepts for CdZnTe Radiation Detectors
CE Lehner, GC Dunham
Pacific Northwest National Laboratory, Richland, Washington

Mesopore Uniformity and Hydrothermal Stability of Silica Thin Films for High Permeability Applications
RE Williford
Pacific Northwest National Laboratory, Richland, Washington

Nano-Porous Titanium Oxide Ceramics
A Bandyopadhyay
Washington State University, Pullman, Washington

X-Ray Photoelectron Spectroscopic Study of CeO_2 and $CeZrO_2$
L Wang, S Azad
Pacific Northwest National Laboratory, Richland, Washington

Fabrication of Microconduits
GC Dunham
Pacific Northwest National Laboratory, Richland, Washington

Development of Advanced Durable Lean NO_x Catalysts for Diesel Engine After Treatment
PW Park, K Koshkarian
Caterpillar, Inc., Alabama

Evaluation of Secondary Ion Mass Spectrometry for Location of Bacterial Spores and to Source Growth Media and Geographic Location
JB Cliff
Pacific Northwest National Laboratory, Richland, Washington

X-Ray Diffraction Analysis of Inorganic Chemicals
AF Fuciarelli
Colorado State University, Fort Collins, Colorado
LL Reed
Battelle Columbus, Richland, Washington

Post-Growth Analysis of GaN and InGaN Grown with Metal Oxide Chemical Vapor Deposition
K Poochinda, T Chen
University of Washington, Seattle, Washington

Crystal Perfection in Cadmium Zinc Telluride Radiation Detectors
MB Toloczko, M Bliss
Pacific Northwest National Laboratory, Richland, Washington

Materials for Automotive Sensor Development
GW Coffey
Pacific Northwest National Laboratory, Richland, Washington

Chemistry of Cadmium Zinc Telluride Surfaces after Processing
AA Rouse, C Szeles
EV Products, Saxonburg, Pennsylvania

X-Ray Diffraction Data Analysis and Consultation
ME Bussell
Western Washington University, Bellingham, Washington

Characterizations of NiAu Bimetallic Butane Steam Reforming Catalyst
Y Chin
Pacific Northwest National Laboratory, Richland, Washington

Synthesis, Characterization, and Evaluation of Molybdenum Phosphide Hydrodesulfurization Catalysts
DC Phillips, DH Shorten, ME Bussell, SJ Sawhill, J King, AW Burns, M Pease, KA Layman, DR Van Wyk
Western Washington University, Bellingham, Washington

Low Angle X-Ray Characterization of Catalyst Porosity
CF Habeger, M Delgado, XS Li, GE Fryxell
Pacific Northwest National Laboratory, Richland, Washington

X-Ray Photoelectron Spectroscopic Characterization of Ion-Beam Induced Surface Modification
J Laskin, AK Shukla, E Denisov
Pacific Northwest National Laboratory, Richland, Washington

Characterization of Solid-State Materials with Planar Carbon Cluster Unit
H Zhang
Washington State University Tri-Cities, Richland, Washington

Scanning Electron Microscopy of Polyaniline/Iron-Hexacyanoferrate Composite Film
Y Lin
Pacific Northwest National Laboratory, Richland, Washington

Growth and Investigation of Cobalt-Doped Anatase Films
U Diebold, K Katsiev, N Ruzycki
Tulane University, New Orleans, Louisiana

Microfabricated Series Connected Electrochemical Potentiometric Oxygen Sensor and Fuel Cell
R Radhakrishnan, AV Virkar
University of Utah, Salt Lake City, Utah
SC Singhal
Pacific Northwest National Laboratory, Richland, Washington

Measurement of Carbon Cluster Emission from Graphite Sputtered by Noble Gas Ions Near Threshold
RE Stevens
Whitworth College, Spokane, Washington
AG Joly
Pacific Northwest National Laboratory, Richland, Washington

Single-Molecule Imaging at Langmuir-Blodgett Bilayers
HP Lu, D Hu
Pacific Northwest National Laboratory, Richland, Washington

Strengthening Mechanisms in Ultra-High-Strength Corrosion Resistant Steel
WE Wood, G Nightingale, G Mares, J Keegan
Portland State University, Portland, Oregon

Copper Interconnect Structure in Field Emission Scanning Electron Microscopy
DP Field, Y Kusama
Washington State University, Pullman, Washington

Auger Electron Spectroscopy Study of Chemical Segregation in the Titanium-Platinum-Lead/Zirconate/Titanate System for Micro-Electro-Mechanical Systems Devices
DF Bahr, LR Eakins
Washington State University, Pullman, Washington

Development of Novel Mass Spectrometry Instrumentation for Real-Time Monitoring of Trace Levels of Volatile Organic Compounds in Air
PT Palmer, W Funk
San Francisco State University, San Francisco, California

Determination of the Factors Controlling Colloid Generation from Altered Waste Forms: Transmission Electron Microscopy Study of Colloid Interactions and Fractal Structure
EC Buck
Pacific Northwest National Laboratory, Richland, Washington

Microstructure Characterization of Platinum on Silicon
BR Johnson
Pacific Northwest National Laboratory, Richland, Washington

New Metal Niobate and Silicotitanate Ion Exchangers: Development and Characterization
L Li
Pacific Northwest National Laboratory, Richland, Washington

Stable Isotopes to Study Nutrient Cycling in Soils
DD Myrold, PJ Bottomley
Oregon State University, Corvalis, Oregon
JB Cliff, CE Lehner
Pacific Northwest National Laboratory, Richland, Washington

Evaluation of Multicomponent Porous Oxide Films
XS Li
Pacific Northwest National Laboratory, Richland, Washington

Characterization of Aluminosilicate Phases Forming Under Low-Silica Conditions
S Mattigod
Pacific Northwest National Laboratory, Richland, Washington

Synthesis, Characterization, and Testing of Novel Materials for Plasma-Catalyst Technology
CS Lee, SH Noh, H Lee, HH Choi, SS Kim, HR Kim
Keimyung University, Dalseo-Gu, Korea, Republic of Korea

Application of Ion Trap Mass Spectrometry for Analysis of Diesel Exhaust Emissions
MR Smith
Pacific Northwest National Laboratory, Richland, Washington

Spectroscopy and Microscopy of Doped TiO_2 Nanocrystalline Materials
DR Gamelin, JD Bryan, P Radovanovic, NS Norberg
University of Washington, Seattle, Washington

Fuel Reforming Catalyst Characterization
PM Irving, Q Ming
Innovatek, Inc., Richland, Washington

Determination of Valance Band Offset in $Sr_2TiO_4/SrTiO_3$ Heterostructures
JH Haeni, DG Schlom
Pennsylvania State University, University Park, Pennsylvania

Investigation of the Oxidation State of Elements in Natural Brannerites
MX Colella
Australian Nuclear Science and Technology Organization, Lucas Heights, Australia
EC Buck
Pacific Northwest National Laboratory, Richland, Washington

Fundamental Studies of Monolayer-Protected Nanoparticles by Gas Chromatography

JW Grate
Pacific Northwest National Laboratory, Richland, Washington
RE Synovec, GM Gross
University of Washington, Seattle, Washington

Epitaxial Growth and Properties of Nanoscale Oxides for Spintronics

D Schmidt, FS Ohuchi, M Olmstead
University of Washington, Seattle, Washington

Nondestructive Carbon Nanotube Modification of Tailored Functionality

LS Fifield, CL Aardahl
Pacific Northwest National Laboratory, Richland, Washington

Interfacing Chip-Based Nano-Fluidic Systems to Surface-Desorption Mass Spectrometry

JS Kuo, G Fiorini, DT Chiu
University of Washington, Seattle, Washington

White Layer Characterization

WE Wood, J Keegan
Portland State University, Portland, Oregon

Dilute Magnetic Semiconducting Oxide Thin Films and Nanostructures

K Krishnan, A Pakhomov, KA Griffin, X Ji
University of Washington, Seattle, Washington

How Desert Varnish Forms

V Kolb
University of Wisconsin-Parkside, Kenosha, Wisconsin
RS Perry, JT Staley, RS Sletten
University of Washington, Seattle, Washington

MeV Ion Irradiation of Non-Ice Solar System Analogue Materials

PM Beauchamp
Jet Propulsion Laboratory, Pasadena, California
TB McCord, GB Hansen
University of Washington, Seattle, Washington
CA Hibbitts
Planetary Science Institute, Pasadena, California

Characterization of Nanocomposites Using Electrochemistry, X-Ray Photoelectron Spectroscopy, Transmission Electron Microscopy, and Scanning Electron Microscopy

X Ye
University of California, San Diego, La Jolla, California

Investigating Electrochemical Properties, Composition, and Oxidation States of Nanoparticles and Catalysts Using Electrochemistry and X-Ray Photoelectron Spectroscopy

C Zhong
State University of New York at Binghamton, Binghamton, New York

Exchange Bias in Fe/MnPd Bilayers

GP Blomqvist, X Ji, K Krishnan
University of Washington, Seattle, Washington

Development of a Capability to Quantify Arsenic in an Adsorbent

S Maheswaran, NN Yadav
University of Western Sydney, Nepean Australia, Penrith South DC, Australia

Automated Suspension Microarray for Microbial Community Profiling

AE Jarrell
Pacific Northwest National Laboratory, Richland, Washington
DP Chandler
Argonne National Laboratory, Argonne, Illinois

Growth and Characterization of Iron-Doped TiO_2 Films

YJ Kim
Hanbat National University (formerly Taejon National University of Technology), Taejon, Korea, Republic of Korea

X-Ray Diffraction and Transmission Electron Microscopy Measurements of Cobalt Nanospheres, Disks, and Rods

M Beerman
University of Washington, Seattle, Washington

Determination of Size Distribution of Thermal Spray Powders and the Tungsten Carbide Particle Size and Distribution Present in These Powders

GA Tewksbury
Portland State University, Portland, Oregon
DG Atteridge
Columbia Basin College, Pasco, Washington

Combinatorial Sputtering Approach to Properties Modification in Polaron Conducting Films

PH Holloway
University of Florida, Gainesville, Florida
RR Owings
National Institute of Standards and Technology, Boulder, Colorado

Continued Investigation into the Spinel Nickel-Cobalt Oxide System

RR Owings
National Institute of Standards and Technology, Boulder, Colorado

Microstructural and Microchemical Analysis of Chalcogenide Nanowires
BR Johnson
Pacific Northwest National Laboratory, Richland, Washington

Reactivity of Primary Soil Minerals and Secondary Precipitates Beneath Leaking Hanford Waste Tanks
W Um
Pacific Northwest National Laboratory, Richland, Washington

Use of EMSL Scanning Microscopy Capabilities to Study Soil Mineral Weathering
Z Balogh, J Dickinson, CK Keller, AL Espana
Washington State University, Pullman, Washington

Scanning Electron Microscopy of Life Stages of Gall Wasps of the Family Cynipidae
JD DeMartini
Humboldt State University, Arcata, California

Magnetics Nanoparticles Characterization
Y Bao
University of Washington, Seattle, Washington

Scanning Electron Microscope Image Acquisition, X-Ray Elemental Analysis
RM Ozanich
Pacific Northwest National Laboratory, Richland, Washington

Morphology of Colloids Formed in Soils Reacted with Simulated Hanford Waste Tank Solutions and the Distribution of Incorporated and Absorbed Cesium in the Colloids
Y Deng, JB Harsh, M Flury
Washington State University, Pullman, Washington

Reaction Specificity of Nanoparticles in Solution
Y Qiang, J Antony
University of Idaho, Moscow, Idaho
RL Penn
University of Minnesota, Minneapolis, Minnesota
A El-Azab, DR Baer, KH Pecher, JE Amonette, EJ Bylaska, BD Kay, M Dupuis
Pacific Northwest National Laboratory, Richland, Washington
PG Tratnyek
Oregon Health Sciences University/Oregon Graduate Institute, Beaverton, Oregon

Hematite Thin Film Preparation for X-Ray Spectroscopic Studies of the Reactivity and Distribution of Lead (II) and Arsenic (V) at Natural Organic Matter/Iron Oxide Interfaces
T Yoon, GE Brown
Stanford University, Stanford, California

Transmission Electron Microscopy for Analysis of Base and Doped Glasses
LA Rogers
Massachusetts Institute of Technology, Cambridge, Massachusetts

Assessment of Toxic Release Inventory Chemical Emission Factors from Munitions by Real-Time Mass Spectrometric Air Monitoring
BT Jobson, ML Alexander
Pacific Northwest National Laboratory, Richland, Washington
CW Spicer
Battelle Columbus, Columbus, Ohio

Texture, Morphology, and Stress in Lead/Zirconate/Titanate Thin Films
DF Bahr, AL Olson, MS Kennedy, JV Martinez, MC Robinson
Washington State University, Pullman, Washington

Uranium (VI) Sorption Onto Hematite Surfaces
D Bosbach, K Dardenne, M Denecke
Institute for Nuclear Waste Management, Karlsruhe, Germany

Confirmation of Silicon-Carbon Bonds in Grafted Monolayers Through X-Ray Photoelectron Spectroscopy
CD Struckman
South Dakota School of Mines and Technology, Rapid City, South Dakota

Experimental Measurements of the Band Offsets of Epitaxial Silicon on $LaAlO_3$ Single Crystals
SA Chambers, JR Williams
Pacific Northwest National Laboratory, Richland, Washington
LF Edge, DG Schlom, V Vaithyanathan
Pennsylvania State University, University Park, Pennsylvania

Structural Characterizations of Biogenic Germanium Oxide Nanospheres
C Chang, G Rorrer, S Liu
Oregon State University, Corvallis, Oregon

Determination of the Bonding of Various Surfactants onto ZrW_2O_8
ED Swanson
South Dakota School of Mines and Technology, Rapid City, South Dakota

Using Nickle-Ion Irradiation for the Development of Advanced Materials for the Next Generation Nuclear Reactor
TR Allen
University of Wisconsin at Madison, Madison, Wisconsin
J Gan
Argonne National Laboratory West, Idaho Falls, Idaho

Characterization of Defects in Nd:YAG Using High-Resolution Transmission Electron Microscopy

DE Eakins, MG Norton
Washington State University, Pullman, Washington

Hydrolytic Stability and Susceptibility of Transition Metal Diolate Complexes and Applications to Green Oxidation

KP Gable
Oregon State University, Corvallis, Oregon

A Theoretical and Experimental Investigation of Multiplet Splitting for Chromium Spectra Generated by X-Ray Photoelectron Spectroscopy

ES Ilton
Pacific Northwest National Laboratory, Richland, Washington
PS Bagus
University of North Texas, Denton, Texas

Characterization of the Manganese Oxidation State with Electron Energy Loss Spectroscopy

EC Buck
Pacific Northwest National Laboratory, Richland, Washington

Characterization and Method Development for the Back-End of the Line Wafer Processing Concepts

TS Zemanian, CR Yonker, JL Fulton, D Matson, BJ Tarasevich, RJ Orth, GE Fryxell, AH Zacher, AJ Carman
Pacific Northwest National Laboratory, Richland, Washington
DJ Hymes
LAM Research Corporation, Fremont, California

Fabrication of a Nanoelectrode Array Base on an Aligned Carbon Nanotube

Y Tu, Z Ren
Boston College, Chestnut Hill, Massachusetts

Oxidation Studies of Coatings for Interconnect Plates in Solid Oxide Fuel Cells

CV Ramana, RJ Smith, AN Kayani
Montana State University, Bozeman, Montana

Nuclear Reaction Analysis of Helium Retention in 6H Silicon Carbide as a Function of Irradiation and Annealing

RJ Smith
Montana State University, Bozeman, Montana

Metallurgical Characterization of Coatings Deposited by Electrospark Deposition

J Keegan, WE Wood, GA Tewksbury
Portland State University, Portland, Oregon

Catalyst Development for Microreactors
PE Gannon
Montana State University, Bozeman, Montana
DR Palo
Pacific Northwest National Laboratory, Richland, Washington

Electrochemical Sensors for Pesticides and Toxic Metals
F Lu
InTec Science, Inc., Brisbane, California

The Synthesis and Characterization of One-Dimensional Nanostructures
H Zhang, L Wang
Washington State University Tri-Cities, Richland, Washington

Solid Phase Transformations in the Hanford Sediments Treated with Aluminum-Rich, Hyperalkaline, and Saline Solutions
NP Qafoku
Pacific Northwest National Laboratory, Richland, Washington

Immobilized Enzymes for Bioremediation and Biosensing
H Jia
University of Akron, Akron, Ohio
J Kim, JW Grate
Pacific Northwest National Laboratory, Richland, Washington
TE Herricks
University of Washington, Seattle, Washington
J Lee, C Lee, K Min, S Chung, H Na
Seoul National University, Seoul, Republic of Korea
M Kim, J Youn
Korea Advanced Institute of Science and Technology, Daejeon, Republic of Korea
S Nair
Pennsylvania State University, University Park, Pennsylvania
H Ahn, BS Kim
Chungbuk National University, Chungbuk, Republic of Korea
B Kim
Gwangju Institute of Science and Technology, Gwangju, Republic of Korea

Joint Catalyst Development
B Liang
Sichuan University, Chengdu, China

Laminar Growth of Ultrathin Metal Films on Oxide Surfaces
J Osterwalder
Universitaet Zuerich-Irchel, Zuerich, Switzerland

Characterization of Biologically Reduced Uranium Particles
BM Peyton, RK Sani
Washington State University, Pullman, Washington

Environmental Scanning Electron Microscopic Analysis of Gas Hydrate and Hydrate-Bearing Sediments
BP McGrail
Pacific Northwest National Laboratory, Richland, Washington
JS Young
W.R. Wiley Environmental Molecular Sciences Laboratory, Richland, Washington

Background Signal Studies with Proton Transfer Reaction-Mass Spectroscopy
HH Westberg
Washington State University, Pullman, Washington

SEM on Electrode Surface/Electrode Preparation and Testing
W Yantasee
Pacific Northwest National Laboratory, Richland, Washington

The Measurements for Nano-Tip'ID
R Zhao
Pacific Northwest National Laboratory, Richland, Washington

Modified Carbon Supports for Aqueous Phase Catalysis: Applications for the Conversion of Glucose and Fermentation Products to Value-Added Chemicals
GE Fryxell, JF White, JG Frye
Pacific Northwest National Laboratory, Richland, Washington

Characterization of Defects in Yttrium Orthovanadate
JB LeBret, MG Norton, JP Winterstein
Washington State University, Pullman, Washington

Development of Catalyst and Membrane Systems for Fuel Processing
PM Irving, Q Ming, HA Edberg
Innovatek, Inc., Richland, Washington

Synthesis and Analysis of Organic Hydroperoxide
ML Alexander, TL Hubler, BT Jobson
Pacific Northwest National Laboratory, Richland, Washington
TG Karl
National Center for Atmospheric Research, Boulder, Colorado

Scanning Probe Microscope Observation of Anatase TiO_2 Films
H Onishi
Kanagawa Academy of Science and Technology, Takatsu-ku, Kawasaki-shi, Japan

Scanning Electron Microscopy and Secondary Ion Mass Spectrometry Analysis of Organic Semiconductor Films Grown Using Liquid Crystal Solvents
DL Patrick, J McLellan
Western Washington University, Bellingham, Washington

Membrane Introduction Proton Transfer Reaction Mass Spectrometry
ML Alexander
Pacific Northwest National Laboratory, Richland, Washington
E Boscaini
University of Innsbruck, Innsbruck, Austria

Determination of the Structure and Properties of $NaAlH_4$ Hydrogen Storage Materials
A El-Azab
Pacific Northwest National Laboratory, Richland, Washington

Characterization of Heat Treated Silicon Carbide Specimens Using Scanning Electron Microscopy
MJ Guinel, MG Norton
Washington State University, Pullman, Washington

X-Ray Photoelectron Spectroscopic Characterization of the Passive Film/Corrosion Products Formed on Carbon Steel and Nickel-Base Alloy in the Yucca Mountain Repository Environment
V Arjunan, J Lamb
University of Nevada, Reno, Reno, Nevada

Characterizing Metal Nanoparticle Nanoassemblies
SR Emory, HR Pugsley
Western Washington University, Bellingham, Washington

Elechemical Sensor for Environmental Monitoring of Pesticides and Toxic Metals
L Bi
Jilin University, Changchun, China

Novel Structures in Nanocrystalline Ceramic Materials
G Zhan
University of California, Davis, Davis, California

High-Resolution Transmission Electron Microscopic Evidences of Stacking Faults in Zeolitic Minerals Formed in Hanford Sediments Reacted with Simulated Tank Waste Solutions
Y Deng
Washington State University, Pullman, Washington

Microbial Biosignatures in Ocean Basalts

MR Fisk, JA Josef
Oregon State University, Corvallis, Oregon

Nanoclusters, Nanomaterials, and Nanotechnology

A Krishna
Louisiana State University, Baton Rouge, Louisiana
X Cui, J Lee
Portland State University, Portland, Oregon
AJ Anderson, WM Cross, T Engstrom
South Dakota School of Mines and Technology, Rapid City, South Dakota
J Antony
University of Idaho, Moscow, Idaho
MJ Guinel, AD LaLonde, L Wang
Washington State University, Pullman, Washington
FS Wilkinson
Western Washington University, Bellingham, Washington
S Maheswaran
University of Western Sydney, Nepean Australia, Kingswood, Australia
JH Willet
University of Montana, Missoula, Montana
A El-Azab, DR Baer
Pacific Northwest National Laboratory, Richland, Washington
Q Liu
Florida State University, Tallahassee, Florida
AP Kouprine
McGill University, Montreal, Quebec, Canada
DW Galipeau
South Dakota State University, Brookings, South Dakota
PB Kulkarni
Carnegie Mellon University, Pittsburgh, Pennsylvania
ML Cotten
Pacific Lutheran University, Tacoma, Washington
DB Allred, SL Tait, LT Ngo, A Tankut, CM Lee, NT Nguyen, JH Wei, MT Zin
University of Washington, Seattle, Washington
S Kothari
University of Tulsa, Tulsa, Oklahoma
J Hickey
University of South Florida, Tampa, Florida
G Cushing, SP Ingole, DP Kulkarni, GP Lee
University of Alaska Fairbanks, Fairbanks, Alaska

Diffusion Study of α-Fe_2O_3/α-Cr_2O_3 (0001) Superlattice

DC Johnson, TM Phung
University of Oregon, Eugene, Oregon

Microelectromagnets
GC Dunham
Pacific Northwest National Laboratory, Richland, Washington

Differential Anomalous Scattering Determination of Cobalt in Anatase in Cobalt-Doped Titania
MF Toney
Stanford Linear Accelerator Center, Menlo Park, California

Electron Microscopic Analysis of Bacterial Co-Cultures
FJ Brockman
Pacific Northwest National Laboratory, Richland, Washington

On-Line Determination of Selected Vapor-Phase Hoffmann List Compounds by Proton Transfer Reaction-Mass Spectroscopy
GM Anderson
Washington State University Tri-Cities, Richland, Washington

Image Iron Oxide Nanoparticles
GR Holtom
Pacific Northwest National Laboratory, Richland, Washington

DC-1 Molecular and Bio-Imprinting
XS Li
Pacific Northwest National Laboratory, Richland, Washington

Silicon Carbide Nanowires and Nanosprings: Processing, Self-Assembly, Characterization, and Properties
D Zhang, DN McIlroy, AI Alkhateeb, J Wei, YA Kranov, H Mahood
University of Idaho, Moscow, Idaho
AD LaLonde
Washington State University, Pullman, Washington

Two-Dimensional Photonic Crystals Grown by Atomic Layer Deposition for Near Infrared and Visible Optoelectronics Applications
D Zhang, DN McIlroy, AI Alkhateeb, J Wei, YA Kranov, H Mahood
University of Idaho, Moscow, Idaho
AD LaLonde
Washington State University, Pullman, Washington

Mechanisms of Sulfur Poisoning of NO_x Absorber Materials
Y Chin
Pacific Northwest National Laboratory, Richland, Washington

Determine Particle Morphology in Ultrasound Assisted Heterogeneous Catalysis
RS Disselkamp
Pacific Northwest National Laboratory, Richland, Washington

Ion-Solid Interactions in Ceramics
WJ Weber, W Jiang
Pacific Northwest National Laboratory, Richland, Washington
L Wang
University of Michigan, Ann Arbor, Michigan
DK Shuh, P Nachimuthu
Lawrence Berkeley National Laboratory, Berkeley, California

Materials and Methods for Multivariate Chemical Vapor Sensing
JW Grate, DL Baldwin, NC Anheier
Pacific Northwest National Laboratory, Richland, Washington

Monolayer Protected Gold Nanoparticle Investigation and Characterization
JW Grate, BP Dockendorff
Pacific Northwest National Laboratory, Richland, Washington
LA Hughes
Southern Oregon University, Ashland, Oregon

Synthesis and Characterization of Novel Nanocrystalline Oxide Film Structures: Interface-Controlled, Self-Assembled Oxide Quantum Dots
A El-Azab, CF Windisch, DR Baer, J Szanyi
Pacific Northwest National Laboratory, Richland, Washington
JF Groves, Y Du, RK Catalano
University of Virginia, Charlottesville, Virginia

Transmission Electron Microscopy Study of Carbon Nanotube Reinforced Polymer-Derived Ceramic Composites
L An, Y Wang
University of Central Florida, Orlando, Florida

Proton Transfer Reaction-Mass Spectroscopic Characterization of Carbon Nanotube Preconcentrators for Trace Chemical Signature Detection
F Zheng
Pacific Northwest National Laboratory, Richland, Washington

Low Energy Sputtering Experiments Using Rutherford Backscattering Spectroscopy
MR Nakles, MT Domonkos
NASA Glenn Research Center, Cleveland, Ohio

Characterization of Noble Metal Catalysts for Hydrogen Production and Purification in Fuel Cell Applications
S Chin, MD Amiridis
University of South Carolina, Columbia, South Carolina

Hydrogen Adsorption Characterization of Carbon Supported Catalyst
F Zheng
Pacific Northwest National Laboratory, Richland, Washington

Characterization of Polymer Thin Films and Arrays
M Yan, J Ren, R Joshi, MB Harnish
Portland State University, Portland, Oregon
Y Chen
Oregon Health Sciences University/Oregon Graduate Institute, Beaverton, Oregon

Fabricate Nanoscale Thin Film Cathode with Sputter Deposition
O Marina
Pacific Northwest National Laboratory, Richland, Washington
Y Lu, S Adler, JR Wilson, L Dunyushkina
University of Washington, Seattle, Washington

Steam Reforming of Methanol over Highly Active and Selective Pd/ZnO Catalyst
RA Dagle
Pacific Northwest National Laboratory, Richland, Washington

Mechanisms for Self Healing in Gastropods: Lessons from Biology – A Case Study of Two Species, *Lavigeria grandis* and *Nucella lamellosa*
KM Hinkley
University of Washington, Seattle, Washington

Field Effect Studies of $Co_xTi_{1-x}O_2$ Thin Films
AS Posadas, J Yau, C Ahn
Yale University, New Haven, Connecticut

TeO_2 Detector Surfaces
FT Avignone
University of South Carolina, Columbia, South Carolina

Particle Size, Associations, and Crystallinity of Bioreduced Uranium Phases
S Fendorf, JM Neiss
Stanford University, Stanford, California

Real-Time Trace Gas Measurements by Chemical Ionization Mass Spectrometry
BT Jobson, ML Alexander
Pacific Northwest National Laboratory, Richland, Washington
MV White
Sacramento City College, Sacramento, California

Elemental Analysis of Bulk Aerosol Samples Collected with a Drum Impactor During the 2003 Mexico City Metropolitan Area Field Study

RS Disselkamp, A Laskin
Pacific Northwest National Laboratory, Richland, Washington
MJ Molina, BM Zuberi, KS Johnson
Massachusetts Institute of Technology, Cambridge, Massachusetts

Continuous Isosorbide Production

JE Holladay
Pacific Northwest National Laboratory, Richland, Washington

Thermogravimetric/Differential Scanning Calorimetry Analysis of Anhydrosugar Samples

JE Holladay
Pacific Northwest National Laboratory, Richland, Washington

New Technologies for Reduction of Automobile Exhaust Emissions

CHF Peden
Pacific Northwest National Laboratory, Richland, Washington
H Zhao
University of Southern California, Los Angeles, California

Silicon Nanotips for Enhanced Electron Emission

GC Dunham, CC McQuerry
Pacific Northwest National Laboratory, Spokane, Washington

Bioavailability of Arsenic in Dislodgeable Residue from Pressure-Treated Wood

BM Sass
Battelle Columbus, Columbus, Ohio

Photovoltaics Projects

GE Fryxell
Pacific Northwest National Laboratory, Richland, Washington

X-Ray Photoelectron Spectroscopic Characterization of Diesel Soot Materials

D Kim
Pacific Northwest National Laboratory, Richland, Washington

Electrochemical and Atomic Force/Scanning Tunneling Microscopy Study of Anatase Film on a $SrTiO_3$ Substrate

L Kavan
J. Heyrovsky Institute of Physical Chemistry, Academy of Sciences of the Czech Republic, Prague, Czech Republic

Oxidation of Iron/Copper and Iron/Silver Multilayer Films Prepared by Direct Current Magnetron Sputtering
AP Kouprine, DU Ryan, Z Altounian
McGill University, Montreal, Quebec, Canada

Characterization of Regenerable Carbon Dioxide Sorbents
F Zheng
Pacific Northwest National Laboratory, Richland, Washington

Chemical Processing of Terpene Emissions from Forests
PV Doskey
Argonne National Laboratory, Argonne, Illinois

Europium Uptake in Various Self-Assembled Monolayer Coated Mesoporous Silica
RS Addleman, ED Bott
Pacific Northwest National Laboratory, Richland, Washington
JT Bays
U.S. Military Academy, West Point, New York

Tunneling Electron Microscopy and X-Ray Photoelectron Spectroscopy Analysis of Ligand-Functionalized Semiconductor Quantum Dots Used in Biodetection Studies
MG Warner, CJ Bruckner-Lea
Pacific Northwest National Laboratory, Richland, Washington

Phenotypic Characterization of Trichloroethylene and Tetrachloroethylene Degrading Dehalococcoides
MR Fisk, AR Sabalowsky, LC Semprini, LB Parker, NW Chambers
Oregon State University, Corvallis, Oregon

Degradation of Oxalate Containing Compounds by Soil Microbes
SA Boyle, DD Myrold
Oregon State University, Corvallis, Oregon

Physical Properties of Natural Siliceous Sinters from Thermal Springs
NW Hinman
University of Montana, Missoula, Montana

Surface Structure and Chemistry of Carbonate Minerals
DR Baer, JE Amonette
Pacific Northwest National Laboratory, Richland, Washington

Ultrapure, Monodisperse, Spherical, Unagglomerated Nano Powders for Infrared Window Materials
A Akash
Ceramatec, Inc., Salt Lake City, Utah

Hydrogen Adsorption/Release Study of Selected Chemical Hydrides
L Li
Pacific Northwest National Laboratory, Richland, Washington

Investigation of Strain in InGaN Multiple Quantum Well Structures
MC Johnson
Lawrence Berkeley National Laboratory, Berkeley, California

Oxidation of Lead Sulfide Surfaces in the Presence of Phosphate: Nanoparticle Formation
AG Stack, WH Casey
University of California, Davis, Davis, California

Transmission Electronic Microscopy and Scanning Electron Microscopy Investigation of Non-Pathogenic Bacterial Cultures
AC Dohnalkova
Pacific Northwest National Laboratory, Richland, Washington

Variable temperature X-Ray Diffraction studies of a Ge/SiO_2/Si System
Y Liang
Motorola, Tempe, Arizona

Observations of Scytonema-Colonized and Non-Colonized Fiber Cement Roofing Shingles
RM Fisher, BA Reine
Lab/Cor, Inc., Seattle, Washington

Magnetic and Transport Studies of Cobalt-Doped TiO_2 Thin Films
A Punnoose
Boise State University, Boise, Idaho

Composition Characterization of ZnO:Cr and ZnO:Co
BK Roberts, K Krishnan
University of Washington, Seattle, Washington

MBE Growth of Epitaxial Anatase TiO_2 (001) on $SrTiO_3$ (001) on Silicon (001) and Characterization of TiO_2 Films
KA Griffin, K Krishnan
University of Washington, Seattle, Washington

Fabrication and Characterization of Functional Nanostructured Materials
S Jin, X Ye
University of California, San Diego, La Jolla, California

Fabrication and Characterization of Carbon Nanotube-Based Composites
S Jin, X Ye
University of California, San Diego, La Jolla, California

Synthesis and Characterization at the Atomic Level of Novel Nanocrystalline Metal Oxide Structures
Z Yu
Nanjing Normal University, Nanjing, China

Surface Analysis of Metal Carbides
Y Shin
Pacific Northwest National Laboratory, Richland, Washington

Analysis of Catalysts and Microchannel Components
VS Stenkamp, KP Brooks, DL King, W Tegrotenhuis, CM Fischer
Pacific Northwest National Laboratory, Richland, Washington

Template-Based Growth of V_2O_5 Nanorods by Electrodeposition and/or Sol Electrophoresis
G Cao
Pacific Northwest National Laboratory, Richland, Washington
SJ Limmer
University of Washington, Seattle, Washington

Scanning Tunneling Microscopic Tip Analysis by Transmission Electron Microscopy
Z Dohnalek
Pacific Northwest National Laboratory, Richland, Washington

Micro-Dimension Calibration
YB Peng
XL Science and Technology, Richland, Washington

Sulfur Absorbents for Emission Control
L Li
Pacific Northwest National Laboratory, Richland, Washington

X-Ray Diffraction Analysis of a Mineral Sample
VC Rundhaug
Columbia Gem and Jewelry, Kennewick, Washington

Synthesis of Gold Nanoclusters
H Zhang, L Wang
Washington State University Tri-Cities, Richland, Washington

Development of a Soldier-Portable Power System
DR Palo
Pacific Northwest National Laboratory, Richland, Washington

Characterization of Surface and Materials
C Lei
Pacific Northwest National Laboratory, Richland, Washington

Scanning Electron Microscope Characterization of Proposed Hydrogen Storage Materials
LE Thomas
Pacific Northwest National Laboratory, Richland, Washington

X-Ray Photoelectron Spectroscopic Analysis of Fuel Cell Components
LR Pederson
Pacific Northwest National Laboratory, Richland, Washington

Investigation of Elemental Contamination in Solid Oxide Fuel Cell Materials
VL Sprenkle
Pacific Northwest National Laboratory, Richland, Washington

Investigation of the Stability of Secondary Precipitates Incorporated with Contaminants
W Um
Pacific Northwest National Laboratory, Richland, Washington

Analysis of Catalysts
DC Elliott
Pacific Northwest National Laboratory, Richland, Washington

Growth of Vanadium Oxides on Anatase TiO_2 (001)
W Gao, EI Altman
Yale University, New Haven, Connecticut

Chalcogenide Surface Science
BR Johnson
Pacific Northwest National Laboratory, Richland, Washington
MH Engelhard
W.R. Wiley Environmental Molecular Sciences Laboratory, Richland, Washington

Characterization of Lithium Aluminate Powders
BR Johnson, TR Hart
Pacific Northwest National Laboratory, Richland, Washington

Hydrogenation of Pyrolysis Oils to Create Value-Added Chemicals
TR Hart, DC Elliott
Pacific Northwest National Laboratory, Richland, Washington

Deposition of Cobalt-Doped Oxides for Spintronic Applications

SA Chambers, TC Droubay
Pacific Northwest National Laboratory, Richland, Washington
S Thevuthasan, DE McCready, V Shutthanandan
W.R. Wiley Environmental Molecular Sciences Laboratory, Richland, Washington
TC Kaspar
University of Washington, Seattle, Washington

Continuous Liquid Feed Flash Evaporation System for Organic Semiconductors

PE Burrows
Pacific Northwest National Laboratory, Richland, Washington

Probing Cation Disordering in $Gd_2Ti_2O_7$ Pyrochlore by X-Ray Photoelectron Spectroscopy

RC Ewing, J Lian
University of Michigan, Ann Arbor, Michigan

Routine Manipulation of Transition Metal Salts in an Inert Atmosphere Glove Box

MG Warner, CJ Bruckner-Lea
Pacific Northwest National Laboratory, Richland, Washington

In Situ X-Ray Photoelectron Spectroscopic Measurements of Reforming Catalysts

V Subramani
Pennsylvania State University, University Park, Pennsylvania

Studies of Corrosion of Materials by Lead Alloys for Advanced Reactor and Nuclear Waste Amelioration Applications

AL Johnson, JW Farley, DJ Koury, DA Parsons, TT Ho, U Younas
University of Nevada, Las Vegas, Las Vegas, Nevada
EP Loewen
Idaho National Laboratory, Idaho Falls, Idaho

Influence of Gadolinium and Samarium Doping on Atomic and Ionic Transport Properties of Novel Nanostructured Ceria-Zirconia Multilayers

A El-Azab, O Marina, C Wang, D Matson
Pacific Northwest National Laboratory, Richland, Washington
S Thevuthasan, L Saraf, V Shutthanandan
W.R. Wiley Environmental Molecular Sciences Laboratory, Richland, Washington

X-Ray Diffraction and Transmission Electron Microscopic Characterization of Magnetic Thin Films

B Pesic
University of Idaho, Moscow, Idaho

Catalyst Characterization
RS Disselkamp
Pacific Northwest National Laboratory, Richland, Washington

Formation of Silicides by Ion Beam Synthesis
HJ Whitlow, CT Jonsson
Lund Institute of Technology, Lund University, Lund, Sweden

Hydrogen Storage
TS Autrey
Pacific Northwest National Laboratory, Richland, Washington

Fundamental Studies of Oxygen Storage Materials
CHF Peden, J Szanyi
Pacific Northwest National Laboratory, Richland, Washington

Fundamental Studies of NO_x Adsorber Materials
CHF Peden, J Szanyi, D Kim, RG Tonkyn
Pacific Northwest National Laboratory, Richland, Washington

Early Transition Metal Oxides as Catalysts: Crossing Scales from Clusters to Single Crystals to Functioning Materials
CHF Peden, Y Wang, JZ Hu
Pacific Northwest National Laboratory, Richland, Washington

Syntheses of Iron-Sulfur Cluster Complexes with Peptides as Terminal Ligands
Y Fu, L Wang
Washington State University, Richland, Washington

Nanotemplated Electrodeposition
DB Allred, DT Schwartz
University of Washington, Seattle, Washington

Temperature-Dependence Adsorption and Reaction of Vapor Molecules on Miniaturized Tin Oxide Sensors
M Su, VP Dravid
Northwestern University, Evanston, Illinois

Conductivity of Functionalized Carbon Nanotube Films
R Khairoutdinov
University of Alaska, Fairbanks, Fairbanks, Alaska

Irradiation Induced Three-Dimensional Ordered Arrays of Nanostructure
L Wang, S Zhu, T Ding
University of Michigan, Ann Arbor, Michigan

Thermogravimetric Mass Spectroscopic Analysis During Annealing of HFO_2 Thin Films in Argon
TM Klein
University of Alabama, Tuscaloosa, Tuscaloosa, Alabama

Study the ZnO/CuInGaSSe Junction by X-Ray Photoelectron Spectroscopy
SN Kundu
Pacific Northwest National Laboratory, Richland, Washington

Characterization of Nanostructured Gas Sorbents by Temperature Programmed Desorption/Fourier Transform Ion Resonance Measurements
F Zheng
Pacific Northwest National Laboratory, Richland, Washington

Liquid Chromatographic Separation Development
Q Luo
Pacific Northwest National Laboratory, Richland, Washington

Develop Stable Bipolar Membranes
JR Bontha
Pacific Northwest National Laboratory, Richland, Washington

Studies of Detector Surfaces
SA Lehn, CJ Barinaga
Pacific Northwest National Laboratory, Richland, Washington

Opto-Magnetic Flow Cell
GC Dunham, H Qiao, TY Colgan
Pacific Northwest National Laboratory, Richland, Washington

Characterization of Sputter Deposited Cobalt-Doped TiO_2 Films
KA Griffin, K Krishnan
University of Washington, Seattle, Washington

Hydrogen Storage of Chemical Hydrides
L Li
Pacific Northwest National Laboratory, Richland, Washington

Crystallization Behavior of Bulk Amorphous Alloy
A Bandyopadhyay, S Bose
Washington State University, Pullman, Washington

Kiln Phosphoric Acid
JA Megy
JDC, Inc., New Cumberland, West Virginia

Auger Electron Microscopy for Use in Classifying the Oxide Content in an Electrospark Deposition Coating of Zirconium
GA Tewksbury, WE Wood
Portland State University, Portland, Oregon

Structural Characterization of Nanoporous Thin Films
Z Dohnalek
Pacific Northwest National Laboratory, Richland, Washington

Surface Studies of Electrocatalysts in Methanol Fuel Cells
KS Kim
Neah Power Systems, Bothell, Washington

Passive Film Stability in Alloy 22
S Seal, D Bera
University of Central Florida, Orlando, Florida
DR Baer, RH Jones, CF Windisch
Pacific Northwest National Laboratory, Richland, Washington

Measurements of Aerosol and Aerosol Precursors During the Summer 2004 Northeast Aerosol Experiment
PH Daum
Brookhaven National Laboratory, Upton, New York

Microcharacterization of Engineered Mono-Sodium Titanate
EC Buck
Pacific Northwest National Laboratory, Richland, Washington

Structure of Combined Colloidal/Organic Fouling Layer on a Nanofiltration Membrane
Q Li
Oregon State University, Corvallis, Oregon

Acid Vapor Weathering of Mars Analog Surface Materials
GB Hansen
University of Washington, Seattle, Washington
CA Hibbitts
Planetary Science Institute, Pasadena, California

Characterization of Nanostructured Ceramics
S Bose
Washington State University, Pullman, Washington

X-Ray Photoelectron Spectroscopy of Materials for Hydrogen Storage
BJ Tarasevich
Pacific Northwest National Laboratory, Richland, Washington

Synthesis of Cu_2O Under Protein Control
H Dai, DT Schwartz
University of Washington, Seattle, Washington

Deposition of Fuel Cell Materials
VL Sprenkle, CA Coyle
Pacific Northwest National Laboratory, Richland, Washington

Yttrium Phosphate/Gadolinum Phosphate Particles for Cancer Imaging and Treatment
A Gutowska
Pacific Northwest National Laboratory, Richland, Washington

Microstructural Investigations of Novel Magnetic Oxide Semiconductors
A Punnoose
Boise State University, Boise, Idaho

Image Polystyrene Microparticles
RM Ozanich
Pacific Northwest National Laboratory, Richland, Washington

Catalysis Collaborative Access Team
CHF Peden
Pacific Northwest National Laboratory, Richland, Washington

Atmospheric Emissions Collaborative Access Team
JM Hales
Envair, Pasco, Washington

Controlled Defect Generation in Porous Silicon
DR Baer
Pacific Northwest National Laboratory, Richland, Washington
FS Ou
State University of New York at Buffalo, Geneseo, New York

ATM, ISO, and Other Standard and Metrology Measurements for Surface Analysis
DR Baer
Pacific Northwest National Laboratory, Richland, Washington

Ion Channeling Studies of Epitaxial Oxide Films and Gas-Solid Interfaces
KR Padmanabhan
Wayne State University, Detroit, Michigan

Soft Lithography for Optics
GC Dunham, JC Birnbaum, CR Batishko, JA Willett
Pacific Northwest National Laboratory, Richland, Washington

Nanomaterial Toxicology
DR Baer
Pacific Northwest National Laboratory, Richland, Washington

Surface Area Measurements
WJ Shaw
Pacific Northwest National Laboratory, Richland, Washington

Aging of Lean NO_x Traps
BG Bunting
Oak Ridge National Laboratory, Knoxville, Tennessee

Characterization of Chromium (III) Solid Phases
D Rai
Pacific Northwest National Laboratory, Richland, Washington

Surface Cleanliness of Silicon Wafer after Laser Treatment
L Scudiero
Washington State University, Pullman, Washington

X-Ray Photoelectron Spectroscopic Studies of Cobalt Phthalocyanine Thin Films
KW Hipps, WA English
Washington State University, Pullman, Washington

Surface Characterization of Calcium Phosphates
WJ Shaw
Pacific Northwest National Laboratory, Richland, Washington

Scanning Electron Microscopy Assessment of Protein-Assisted Calcium Phosphate Nucleation
WJ Shaw
Pacific Northwest National Laboratory, Richland, Washington

Origin of the Face Dependent Photocatalytic Activity of TiO_2: Probing Surface Chemistry with Molecular Adsorption
U Diebold, TJ Beck, A Klust
Tulane University, New Orleans, Louisiana
MA Henderson
Pacific Northwest National Laboratory, Richland, Washington

Photochemical Studies on N-Doped TiO_2 Single Crystals
MA Henderson
Pacific Northwest National Laboratory, Richland, Washington
MD Robbins, JM White
University of Texas at Austin, Austin, Texas

Size Selected Gas-Phase Soot Aerosol Oxidation

SH Kim
National Institute of Standards and Technology, Gaithersburg, Maryland
MR Zachariah
University of Maryland, Gaithersburg, Maryland

Scanning Electronic Microscope Image of Microparticles

RM Ozanich
Pacific Northwest National Laboratory, Richland, Washington

X-Ray Photoelectron Spectroscopic Analysis on Tungsten Oxide Nanoclusters Supported on MCM41

JE Herrera
Pacific Northwest National Laboratory, Richland, Washington

Chrome Volatility

GD Maupin
Pacific Northwest National Laboratory, Richland, Washington

Liquid Product Analysis by Gas Chomatography and Mass Spectrometry

J Hu
Pacific Northwest National Laboratory, Richland, Washington

Tungsten Analysis as a Surrogate for Uranium in Ash

TR Hart, AJ Schmidt, MR Elmore
Pacific Northwest National Laboratory, Richland, Washington

Inductively-Coupled Plasma Spectrometer Analysis of Metal Ions

W Yantasee
Pacific Northwest National Laboratory, Richland, Washington

Structure and Property Tailoring of Metal Nanoparticles Dispersed in Dielectrics by High-Energy Ion Implantation

C Wang, S Thevuthasan, V Shutthanandan
W.R. Wiley Environmental Molecular Sciences Laboratory, Richland, Washington
G Duscher
North Carolina State University, Raleigh, North Carolina

New Materials as Sulfur Absorbents

L Li
Pacific Northwest National Laboratory, Richland, Washington

Structure and Performance of DNA Biosensors

CJ Bruckner-Lea, T Staub
Pacific Northwest National Laboratory, Richland, Washington

AS Lea
W.R. Wiley Environmental Molecular Sciences Laboratory, Richland, Washington

Surface Analysis of Indoor Air Quality Volatile Organic Carbon Sensors
M Kleefstra
AirAdvice Inc., Portland, Oregon

Characterization of Aluminum Nitride-Silicon Carbide Alloy Crystals on Silicon Carbide Substrates
JH Edgar, Z Gu
Kansas State University, Manhattan, Kansas

Surface State Characterization of Pt/Al_2O_3 Catalyst for the Catalytic Partial Oxidation Reaction
KL Hohn, C Cao
Kansas State University, Manhattan, Kansas

Gas Cell Metallization
KC Antolick, JI McIntyre, GC Dunham
Pacific Northwest National Laboratory, Richland, Washington

Interposer Profile Measurements
LE Bowman
University of Alaska, Fairbanks, Fairbanks, Alaska

Chemical Analysis of Nano-Structures for Toxic Gas Detection
DW Galipeau
South Dakota State University, Brookings, South Dakota

Synthesis and Characterization of Enzyme Nanoparticles
G Liu
Pacific Northwest National Laboratory, Richland, Washington

Mesopore Uniformity and Hydrothermal Stability of Silica Thin Films for High Permeability Applications
S Li, A Qiao
Pacific Northwest National Laboratory, Richland, Washington

Determination of Pore Structure in Highly Porous Silica Oxide Powders
LS Fifield, RD Champion
Pacific Northwest National Laboratory, Richland, Washington

Characterization of Corrosion Products on Iron Aluminide Coated Alloys
DJ Senor
Pacific Northwest National Laboratory, Richland, Washington

Salt Cake Waste Fractional Crystallization and Displacement Washing

GB Josephson, JG Geeting
Pacific Northwest National Laboratory, Richland, Washington

Surface Assessment of B_xC_y Thin Film on Silicon

AJ Carman
Pacific Northwest National Laboratory, Richland, Washington

Electroforming Copper

GC Dunham
Pacific Northwest National Laboratory, Richland, Washington

X-Ray Photoelectron Spectroscopic Investigations of Transition Metal Doped Oxide Semiconductors

J Hays, A Punnoose
Boise State University, Boise, Idaho

Effects of Ice-Clearing Chemicals

EV Stephens
Pacific Northwest National Laboratory, Richland, Washington

Testing of Carbon-Based Materials for Hydrogen Storage

G Cao
Pacific Northwest National Laboratory, Richland, Washington
AM Feaver
University of Washington, Seattle, Washington

Staff

S. Thevuthasan, Staff Scientist, Technical Lead
(509) 376-1375, theva@pnl.gov

Barbara L. Diehl, Administrator
(509) 376-1518, barb@pnl.gov

Lisa Smith, Administrator (January 2004 - October 2004)
(509) 376-1518, l.smith@pnl.gov

Marisol Avila, Technician
(509) 376-1833, marisol.avila@pnl.gov

Mark H. Engelhard, Research Scientist
(509) 376-1664, mark.engelhard@pnl.gov

Daniel J. Gaspar, Senior Research Scientist (See also IDL)
(509) 376-2413, daniel.gaspar@pnl.gov

A. Scott Lea, Senior Research Scientist
(509) 376-9145, scott.lea@pnl.gov

Igor V. Lyubinetsky, Senior Research Scientist
(509) 376-5220, igor.lyubinetsky@pnl.gov

David E. McCready, Research Scientist
(509) 376-9648, david.mccready@pnl.gov

Laxmikant V. Saraf, Senior Research Scientist
(509) 376-2006, laxmikant.saraf@pnl.gov

V. Shutthanandan, Senior Research Scientist
(509) 376-2708, shuttha@pnl.gov

Chongmin Wang, Scientist
(509) 376-4292, chongmin.wang@pnl.gov

We would also like to acknowledge the contributions from Gregory J. Exarhos, Charles H.F. Peden, Donald R. Baer, Jay W. Grate, Scott A. Chambers, William J. Weber, Michael A. Henderson, Janos Szanyi, Do Heui Kim, Michael L. Alexander, Timothy C. Droubay, Weilin Jiang, Alice Dohnalkova, Mark E. Gross, Ya-Huei Chin, Yong Wang, Yuehe Lin, Timothy L. Hubler, Todd R. Hart, Robert T. Rozmiarek, and Jungbae Kim.